Fault-valve instability: A mechanism for slow slip events

So Ozawa[1], Yuyun Yang[2], Eric M. Dunham[1,3]

[1]Department of Geophysics, Stanford University
[2]Earth and Environmental Sciences Programme, The Chinese University of Hong Kong
[3]Institute for Computational and Mathematical Engineering, Stanford University

Key Points:

- We analyze the dynamics of fault slip with fault-zone fluid flow and fault-parallel permeability enhancement with slip and sealing with time
- Fault-valve instability produces unidirectional aseismic slip and pore pressure pulses even with velocity-strengthening friction
- Subduction zone earthquake cycle simulations show that the fault-valve instability can produce slow slip events below the seismogenic zone

Corresponding author: So Ozawa, sozawa@stanford.edu

Abstract

Geophysical and geological studies provide evidence for cyclic changes in fault-zone pore fluid pressure that synchronize with or at least modulate seismic cycles. A hypothesized mechanism for this behavior is fault valving arising from temporal changes in fault zone permeability. In our study, we investigate the coupled dynamics of rate and state friction, along-fault fluid flow, and permeability evolution. Permeability decreases with time, and increases with slip. Linear stability analysis shows that steady slip with constant fluid flow along the fault zone is unstable to perturbations, even for velocity-strengthening friction with no state evolution, if the background flow is sufficiently high. We refer to this instability as the "fault valve instability." The propagation speed of the fluid pressure and slip pulse can be much higher than expected from linear pressure diffusion, and it scales with permeability enhancement. Two-dimensional simulations with spatially uniform properties show that the fault valve instability develops into slow slip events, in the form of aseismic slip pulses that propagate in the direction of fluid flow. We also perform earthquake sequence simulations on a megathrust fault, taking into account depth-dependent frictional and hydrological properties. The simulations produce quasi-periodic slow slip events from the fault valve instability below the seismogenic zone, in both velocity-weakening and velocity-strengthening regions, for a wide range of effective normal stresses. A separation of slow slip events from the seismogenic zone, which is observed in some subduction zones, is reproduced when assuming a fluid sink around the mantle wedge corner.

Plain Language Summary

Slow slip events are observed in subduction zones worldwide. Their mechanism is not well understood, but geophysical and geological research suggests a relation with recurring changes in fluid pressure within the fault zone. Here we explore the fault valve mechanism for slow slip events using mathematical and computational models that couple fluid flow through fault zones with frictional slip on faults. The fault valve mechanism produces pulses of high fluid pressure, accompanied by slow slip, that advance along the fault in the direction of fluid flow. We quantify the conditions under which this occurs as well as observable properties like the propagation speed and rate of occurrence of slow slip events. We also perform simulations of subduction zone slow slip events using fault zone and frictional properties that vary with depth in a realistic manner. The

simulations show that the fault valve mechanism can produce slow slip events with approximately the observed rate of occurrence, while also highlighting some discrepancies with observations that must be addressed in future work.

1 Introduction

Tectonic faults slip both seismically and aseismically. In this century, we have become increasingly confident that aseismic slip is a ubiquitous phenomenon worldwide, especially along subduction megathrusts (Nishikawa et al., 2019; Bürgmann, 2018). Slow slip events (or, more generally, slow earthquakes) have much slower slip rates than ordinary earthquakes, but what limits their slip rate remains unclear. What determines the spatial distribution of fast and slow earthquakes is also an open question.

The recurrent nature of slow slip events is easily explained by the concept of stick-slip. Rate and state friction laws are widely used to explain stick-slip behavior and earthquake cycles (Dieterich, 1979; Marone, 1998; Tse & Rice, 1986; Scholz, 1998). There are two prevailing models for slow slip events based on rate and state friction laws. In the absence of elastic or poroelastic bimaterial effects, steady slip is always stable for a velocity-strengthening fault and is conditionally unstable for a velocity-weakening fault (Ruina, 1983; Rice et al., 2001) (Figure 1a). Slow slip occurs on a velocity-weakening fault when the fault length is near the critical wavelength for instability (Liu & Rice, 2007), which we refer to as the neutral stability model. In other words, the nucleated earthquake arrests before it becomes a fast rupture. The main criticism of this model is that the parameter range of slow slip occurrence is very narrow (Rubin, 2008), especially when the slip law is used for state evolution. Heterogeneous frictional properties, geometrical complexity, and dilatant strengthening are often invoked to broaden the parameter range that produces slow slip events (Nie & Barbot, 2021; Skarbek et al., 2012; Romanet et al., 2018; S. W. Ozawa et al., 2019; Segall et al., 2010).

The other prevailing model to generate slow slip is the transition from velocity weakening to velocity strengthening friction at an imposed critical velocity (Shibazaki & Iio, 2003; Kato, 2003; Matsuzawa et al., 2013; Im et al., 2020; Hawthorne & Rubin, 2013). The acceleration of slip is limited due to the increase in frictional resistance, which allows slow propagation of the rupture. However, the transition from velocity-weakening to velocity-strengthening friction around the peak slip rate of slow slip events is not uni-

versally observed in laboratory experiments (see Shimamoto (1986); Shreedharan et al. (2022); Okuda et al. (2023); Bar-Sinai et al. (2014) and references therein).

Fluids are thought to be important for slow slip because they are abundant in the regions where slow earthquakes occur. Mechanically, fluid pressure controls fault slip by changing the effective normal stress of the fault. High fluid pressure at the source regions of slow slip is suggested by several observations (Peacock et al., 2011; C. Condit & French, 2022; Kodaira et al., 2004), although the actual value of effective stress is not well constrained. The tidal sensitivity of low-frequency earthquakes requires very low effective normal stress when interpreted within the framework of rate and state friction (Thomas et al., 2012). The two prevailing models for slow slip as mentioned above also require low effective normal stress to reproduce the low stress drop ($\sim$10 kPa) of slow slip events (Gao et al., 2012). The high Vp to Vs ratio obtained from seismic tomography at source regions of slow slip is consistent with high fluid pressure in laboratory experiments (Peacock et al., 2011), although a more recent study suggests that the relationship between fluids and Vp to Vs ratio is not so simple (Brantut & David, 2019).

Many lines of evidence indicate that fluid pressure in the megathrust varies with time (Warren-Smith et al., 2019; Otsubo et al., 2020). For example, fluid pressure variations estimated from focal mechanisms of earthquakes in megathrust regions are correlated with the cycle of slow slip (Warren-Smith et al., 2019). S-wave velocity measurements show a change of about 0.1 km/s during slow slip events (Gosselin et al., 2020). Gravity changes have also been explained by fluid migration during slow slip events (Tanaka et al., 2018). More direct evidence comes from exhumed outcrops. Crack-seal textures observed in veins suggest cyclic variations in pore fluid pressure (Ujiie et al., 2018; C. Condit & French, 2022). The existence of extensional and shear veins in the same direction requires cyclic changes in the direction of σ_1 and σ_3. Using a poroelastic model of vein formation, Otsubo et al. (2020) estimated that the variation in fluid pressure is 7-8% of the total fluid pressure in a seismic cycle. In the laboratory, cyclic pore fluid pressure changes during stick-slip cycles have been directly observed (Brantut, 2020; Proctor et al., 2020).

Several mechanisms have been proposed to explain the cyclic variation of pore fluid pressure. The fault valve model proposed by Sibson (1992) has received much attention for a long time. In this model, the permeability along a fault is low during the interseis-

mic period, so that fluid overpressure develops below the seismogenic zone in response to continued fluid influx from depth. Once the fault slips in an earthquake, in part due to the weakening caused by fluid overpressure, permeability increases as a result of the dilation of fault gouge and the generation of microfractures. This allows upward flow and at least partially relieves the overpressure below the seismogenic zone during the post-seismic period. After the earthquake, the permeability decreases, which again leads to fluid overpressure. This process, in addition to the accumulation and release of shear stress, controls the earthquake cycle. The fault valve model has been invoked to explain the upward migration of seismic swarms (Shelly et al., 2016; Matsumoto et al., 2021; Ross et al., 2020). Farge et al. (2021, 2023) studied the dynamics of transient flow caused by rupture of an impermeable seal and related it to low-frequency earthquakes and tremors.

The fault valve model requires a significant change in permeability with slip and time. There are several lines of evidence supporting this (Saffer, 2012; Ingebritsen & Manning, 2010). The evolution of aseismic slip on a fault during fluid injection experiments on shallow (<1 km depth) faults is best explained by an order of magnitude increase in permeability after slip onset (Bhattacharya & Viesca, 2019; Cappa et al., 2022). It is clear from these experiments that aseismic slip is sufficient to significantly increase the permeability of the fault. Laboratory measurements of fracture permeability show an increase in permeability after increasing the slip rate of the fault (Im et al., 2019). Furthermore, in the shallow megathrust, geochemical and thermal anomalies observed at seepage sites and boreholes yield permeabilities in the range of $10^{-13}\mathrm{m}^2$ (Saffer, 2012). These values are much higher than the time-averaged permeability estimates of $\sim 10^{-15}\mathrm{m}^2$ based on steady-state numerical modeling considering the fluid source of sediment compaction and mineral dehydration (Skarbek & Saffer, 2009). This requires a transient increase in permeability by orders of magnitude. On the other hand, permeability decreases during the interseismic period due to closure of fractures by high normal stress and precipitation of minerals from fluid (Giger et al., 2007; Yehya & Rice, 2020; Xue et al., 2013; Saishu et al., 2017; Fisher et al., 2019; Williams & Fagereng, 2022).

Fluid sources from depth are also required in the fault valve model. At shallow depths of the megathrust, sediment compaction is the main source of fluid (Saffer & Tobin, 2011). In the deeper region, dehydration from metamorphic and metasomatic reactions (Van Keken et al., 2011; Tarling et al., 2019) and mantle-derived fluid (Kennedy et al., 1997; Nishiyama et al., 2020) are the relevant sources of fluid. Fluid pressurization from these sources leads

to fluid overpressure, and because the gradient of fluid pressure is greater than hydrostatic, fluid migrates upward. As evidence, lithostatic fluid pressure gradient is estimated from P-wave velocity measurement below a kilometer depth of the megathrust (Saffer & Tobin, 2011). Rice (1992) shows that lithostatic fluid pressure gradient (and hence depth-independent effective normal stress) occurs when there is fluid flow from depth, and permeability decreases with increasing effective normal stress. Recently, Kaneki and Noda (2023) has developed a more realistic model for determining the fluid pressure distribution in the shallow portion of subduction zones, taking into account reaction kinetics of the smectite-illite transition that is accompanied by fluid release.

As demonstrated by this discussion, fault valving is thought to be important in influencing seismicity and motivates us to build quantitative models of fault slip that account for fault valving processes. If effective normal stress and slip are coupled, velocity-strengthening faults could also develop instability. For example, slip between elastically or poroelastically dissimilar materials generates changes in effective normal stress and destabilizes slip (Rice et al., 2001; Dunham & Rice, 2008; Heimisson et al., 2019). Normal stress changes due to free surface effects can also destabilize slip (Aldam et al., 2016; Ranjith, 2014). In this paper, we present another mechanism for sliding instability on a velocity-strengthening fault based on the fault valve model.

We close this introduction with a conceptual explanation of the fault valve instability. Consider steady sliding and constant flow, which is perturbed by a local increase in slip rate. This locally increases the permeability. If background flow is present, the permeability gradients on either side of the perturbation creates a fluid flow gradient. The negative flow gradient on the downstream side of the perturbation leads to fluid accumulation and increases the fluid pressure. If the shear stress remains relatively constant, then the friction coefficient also increases. The increase in friction coefficient, for velocity-strengthening faults or simply through the direct effect, increases the slip velocity on the downstream side of the initial slip velocity perturbation. This is a positive feedback that promotes instability growth and propagation in the direction of flow (Figure 1a). However, there are processes which can counteract and even prevent the instability. Slip induces a reduction in shear stress through the elastic response of the solid. The reduction is shear stress acts to decrease slip velocity. Similarly, along-fault pressure diffusion can reduce the destabilizing pressurization. An important contribution of

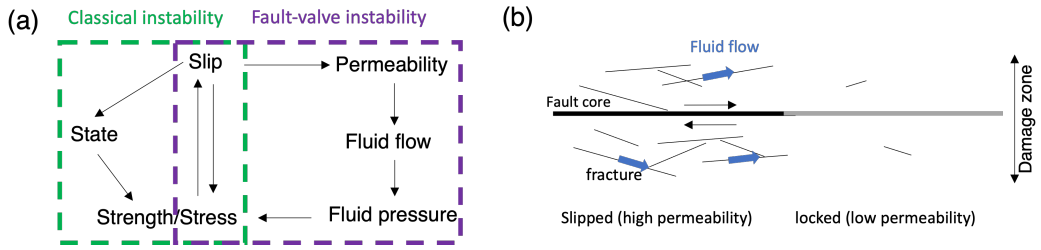

Figure 1. (a) Concepts of both classical and fault-valve instability are shown with the relationship between different variables. (b) Schematic of fault zone structure and fluid flow. The fluid flows through fractures in a fault damage zone that is much wider than the fault core. Permeability is higher in the slipped region than unslipped region.

our work is quantifying the conditions for instability and the role of these various processes in promoting or inhibiting the instability.

We also remark that the fault valve instability is a general instability mechanism that most likely occurs for a broad class of permeability evolution laws. Recently, Zhu et al. (2020) introduced a specific, ad hoc permeability evolution law and demonstrated the emergence of swarm-like seismicity and quasi-periodic slow slip events that propagate up-dip (in the direction of fluid flow), using earthquake sequence simulations. In this study, we show that the emergence of instability occurs for any permeability evolution law for which permeability evolves with slip or time toward a steady-state permeability that depends on slip rate. The instability also requires either a non-zero direct effect or purely velocity-strengthening friction. As friction switches from velocity-strengthening to velocity-weakening, the fault valve instability transitions into the classical rate-state instability that is driven by frictional weakening. Overall, this work demonstrates the destabilization of steady fault sliding and fluid flow for a sufficiently large background flow rate and permeability enhancement, regardless of the velocity dependence of friction.

2 Governing Equations

2.1 Fluid pressure diffusion

We assume that fluid flow is confined within the fault zone and do not consider fault-normal flow (Figure 1b). This assumption is often justified for three reasons.

First, fault damage zones typically have higher permeability and storage compared to the host rock due to the high density of fractures (Wibberley & Shimamoto, 2003; Lockner et al., 2009; Faulkner et al., 2010). In shallow megathrusts, permeabilities three to six orders of magnitude higher than the host rock are required to explain the geochemical and thermal anomalies observed in seepage and borehole studies (Saffer, 2012). This high contrast is not obvious in the deeper plate boundary shear zone where deep slow slip events occur, but there are several field observations of exhumed subduction zones showing that the plate boundary has higher permeability than the surrounding rock (Bebout & Penniston-Dorland, 2016). Even with a high permeability contrast between the fault zone and the host rock, this assumption is only valid if the time scale of interest is shorter than the time required for fluids to leak into the host rock (Yang & Dunham, 2021).

Second, the highly anisotropic permeability resulting from the development of foliated structures with accumulated slip and shearing leads to a significant permeability contrast between fault-parallel and fault-normal directions (Kawano et al., 2011). This will further restrict fault-normal flow.

Third, the time scale of interest is longer than the characteristic fault-normal diffusion time within the highly permeable damage zone, resulting in a uniform fluid pressure across the damage zone. However, it should be noted that the permeability of fault cores is usually much lower than that of damage zones. Therefore, our assumption may not hold if the slip zone is highly localized within the impermeable fault core (Rice, 2006).

When flow is confined to the fault zone and fault-normal flow is neglected, the width of the fault zone is constant, and the mechanical response of the matrix is linear elastic, the fluid pressure diffusion equation is

$$\beta\phi\frac{\partial p}{\partial t} = \frac{\partial}{\partial x}\left(\frac{k}{\eta}\frac{\partial p}{\partial x}\right), \tag{1}$$

where β is the sum of the pore and fluid compressibilities, ϕ is the porosity, k is the permeability, and η is the fluid viscosity. The fluid pressure p is interpreted as overpressure (fluid pressure minus hydrostatic pressure) if some component of gravity is present in the direction of x. The values of $\beta\phi$ and k should be interpreted as the average in the fault-normal direction across the width of the damage zone (Yang & Dunham, 2023), which is typically much wider than the thickness of the localized inelastic shear deformation that accommodates slip.

Note that some models make the opposite assumption: retaining fault-normal diffusion and neglecting fault-parallel diffusion (Segall et al., 2010; Rice, 2006). This is justified when the time scale of interest is shorter than the characteristic diffusion time across the width of the fault zone. Accounting for both fault-parallel and fault-normal diffusion leads to a more complicated set of equations, and would be an important future extension of our model (see also Heimisson et al. (2022)).

There are well-established relationships between permeability k and porosity ϕ in rock physics (Mavko et al., 2020). In this study we assume that ϕ remains constant (except for its small elastic variations captured in the compressibility β) even though the permeability evolves with time. Our underlying assumption is that changes in permeability result from changes in tortuosity (i.e., pore connectivity) rather than from changes in porosity. If porosity were changing in an inelastic manner, a suction or source term would be added to equation (1). The importance of this additional term would depend on the sensitivity of the permeability to changes in porosity. Similar assumptions were made by Zhu et al. (2020) and Dublanchet and De Barros (2021). It is an important future study to include both inelastic porosity and tortuosity changes to explore more realistic situations and to quantify the relative importance of these two mechanisms for permeability evolution. That said, it seems impossible to explain the order of magnitude or larger changes in permeability that are routinely invoked for fault valving through standard relations between k and ϕ (see discussion in Yang and Dunham (2023)).

2.2 Permeability evolution

Many experiments reveal that permeability decreases with increasing effective normal stress σ_e (total normal stress minus pore fluid pressure) because of elastic deformation of pores (David et al., 1994). We account for this through a general relation of the form

$$k = k^* f(\sigma_e), \tag{2}$$

A commonly used parameterization that is consistent with many laboratory experiments is

$$f(\sigma_e) = e^{-\sigma_e/\sigma^*}. \tag{3}$$

The stress sensitivity parameter σ^* is typically of order 10 MPa for fault zone rocks (Mitchell & Faulkner, 2012; Wibberley & Shimamoto, 2003).

Cruz-Atienza et al. (2018) used the same equation with fixed k^* and showed a wave-like solution to the nonlinear pressure diffusion equation, and suggested that the resulting pressure pulse might trigger tremor. In our simulation starting from the steady state, however, the effect of this term is small in comparison to the permeability change from the evolution law for k^* presented below. On the other hand, the value of σ^* is critically important in the steady-state effective normal stress profile in the depth-dependent problem, as shown in Section 5.

Permeability also evolves with slip and time (Im et al., 2019; Zhu & Wong, 1997; Cappa et al., 2022; Ishibashi et al., 2018; Giger et al., 2007; Morrow et al., 2001). We assume a general form for permeability evolution:

$$\frac{dk^*}{dt} = g(k^*, V). \tag{4}$$

As an example of the permeability evolution law, Zhu et al. (2020) introduced

$$g(k^*, V) = \frac{V}{L}(k_{\max} - k^*) + \frac{1}{T}(k_{\min} - k^*). \tag{5}$$

We use this law in our nonlinear earthquake sequence simulations. The first term represents the increase of k^* towards $k_{\max}$ by processes such as microfracturing (Figure 1b). The constant L characterizes the slip distance required for the permeability increase. The second term is the exponential decrease with time toward $k_{\min}$ due to healing and sealing of the microfractures. Some laboratory experiments support the exponential decay of permeability (Giger et al., 2007), but others show a power-law decay (Im et al., 2019). At steady state, k^* is an increasing function of velocity:

$$k^*_{ss}(V) = \frac{k_{\max} + k_{\min} L/TV}{1 + L/TV}. \tag{6}$$

From equation (6), $k_{ss} \sim k_{max}$ for $T > L/V_0$ and healing is too slow to be effective. We use a very small value for k_{min} so that this value does not affect the result. There are four parameters in equation (5). The healing time T is assumed to be about one year from some observations at about 1 km depth (Xue et al., 2013), but depends on the temperature from laboratory experiments (Giger et al., 2007; Morrow et al., 2001). The slip distance L is more difficult to constrain, but Im et al. (2019) reports L to be about 1 mm in slide-hold-slide experiments. It is not necessary to be the same as d_c in rate and state friction because our permeability is considered to be averaged across the fault damage zone.

2.3 Friction

We use the regularized rate and state friction law, and state evolution is governed by the aging law (Dieterich, 1979; Ruina, 1983), in which

$$\frac{\tau}{\sigma_e} = a\text{sinh}^{-1}\left(\frac{Ve^{-\psi/a}}{2V_0}\right), \tag{7}$$

$$\frac{d\psi}{dt} = \frac{b}{d_c}\left(V_0 e^{\frac{f_0-\psi}{b}} - V\right), \tag{8}$$

where τ is the shear stress, ψ is the state variable, f_0 is the reference friction coefficient, a is the coefficient of the direct effect, b is the coefficient of the evolution effect, and d_c is the characteristic slip distance. This form is used in the numerical simulations.

3 Linear stability analysis

We investigate the stability of the system in the previous section to small perturbations about steady state. Steady state quantities are denoted with a subscript 0. Sliding occurs on a planar fault in a homogeneous solid whole-space. The solid response is linear isotropic elastic and we neglect inertia because of our focus on slow slip. The analysis to follow applies equally to antiplane shear and plane strain perturbations, with the elastic modulus μ^* appearing in the relation between shear stress and slip being equal to the shear modulus for antiplane shear and the shear modulus divided by one minus Poisson ratio for plane strain. In this steady state, the fault is sliding at the loading velocity V_0 and the fluid flow rate q_0 is uniform:

$$q_0 = -\frac{k_0}{\eta}\frac{dp_0}{dx}. \tag{9}$$

Without loss of generality, we assume $q_0 > 0$, i.e., fluids flow in the positive x direction in steady state. The unperturbed effective normal stress, σ_0, is spatially uniform. We perform the linear stability analysis for the general form of the permeability evolution and the rate-and-state friction law.

The permeability evolution law (4) and (5) linearizes about the steady state as (see Appendix)

$$\frac{dk}{dt} = -\frac{k_0}{\sigma^*}\frac{d\sigma_e}{dt} - \frac{1}{T_k}\left[k - k_{ss}^{lin}(V,\sigma_e)\right], \tag{10}$$

$$k_{ss}^{lin}(V,\sigma_e) = k_0 - k_0\frac{\sigma_e - \sigma_0}{\sigma^*} + \Delta k\frac{V - V_0}{V_0}, \tag{11}$$

where V is slip velocity, T_k is the time scale for the linearized permeability evolution law, Δk is the characteristic change in permeability, and σ^* is the stress sensitivity parameter characterizing the dependence of permeability on effective normal stress.

The rate and state friction law is also linearized (Rice et al., 2001):

$$\frac{\mathrm{d}\tau}{\mathrm{d}t} = \frac{a\sigma_0}{V_0}\frac{\mathrm{d}V}{\mathrm{d}t} + f_0\frac{\mathrm{d}\sigma_e}{\mathrm{d}t} - \frac{V_0}{d_c}\left[\tau - \tau_{ss}(\sigma_e, V)\right], \tag{12}$$

$$\tau_{ss}(\sigma_e, V) = \tau_0 + f_0(\sigma_e - \sigma_0) + (a-b)\sigma_0\frac{V - V_0}{V_0}. \tag{13}$$

We choose the reference state to be identical to the steady state. The frictional strength τ changes with fluid pressure p via the effective stress law. Laboratory experiments show that this law does not hold instantaneously, at least for changes in total normal stress (Linker & Dieterich, 1992). After the step in effective normal stress, a finite displacement is required to reach the new shear strength expected from the same friction coefficient.

3.1 Characteristic equation

We seek a solution for $\exp(st + i\kappa x)$ perturbations for real-valued wavenumbers κ. Except in special limits, there is more than one solution. The system is unstable when the maximum value of Re(s) is positive, and the perturbation grows with time. We derive the relationship between wavenumber κ and the dimensionless growth rate $S = sT_k$. According to Appendix, the characteristic equation is

$$PS^2 + \left(\frac{a-b}{a}PJ + 1\right)S + J + iPQ\frac{S(S+J)}{(S+1)(S+R+iM)} = 0, \tag{14}$$

with five dimensionless parameters defined as follows:

$$P = \frac{2a\sigma_0}{\mu^*|\kappa|V_0T_k}, \tag{15}$$

$$Q = \frac{\kappa f_0 q_0 \Delta k T_k}{k_0\beta\phi a\sigma_0}, \tag{16}$$

$$R = c_0\kappa^2 T_k, \tag{17}$$

$$M = \frac{\kappa q_0 T_k}{\sigma^*\beta\phi}, \tag{18}$$

$$J = \frac{V_0 T_k}{d_c}. \tag{19}$$

The final, sixth dimensionless parameter, a/b, determines if friction is velocity weakening or velocity strengthening. The parameters P and Q can be understood as the dimensionless ratios of three characteristic shear stress changes. The stress change associated

with the direct effect is $a\sigma_0$. Over the permeability evolution timescale T_k, slip $V_0 T_k$ accrues. Spatial variations of this slip with wavenumber $|\kappa|$ produce an elastic shear stress change $\mu^*|\kappa|V_0 T_k/2$. Finally, the reduction in shear strength from the fault valve effect described at the end of the Introduction is $(\kappa f_0 q_0 \Delta k T_k)(k_0 \beta\phi)$. This can be understood as follows. Linearization of the divergence of fluid flux term in (1) provides a term $(q_0/k_0)\partial k/\partial x \sim q_0\kappa\Delta k/k_0$, which is interpreted as the rate of fluid accumulation from spatial variations in fluid flux caused by spatial variations in permeability. Dividing the fluid accumulation rate by the specific storage $\beta\phi$ gives the pressurization rate. Multiplying this by the permeability evolution timescale T_k gives the pressure change, and multiplying this by f_0 gives the resulting reduction in shear strength. Thus, P compares the direct effect to the elastic stress change, and Q compares the strength reduction from fault valving to the direct effect. In addition, R quantifies the mitigating effect of pressure diffusion by comparing the diffusion length over the permeability evolution timescale, $\sqrt{c_0 T_k}$, to the length scale of the perturbation κ^{-1}. M quantifies the dependence of permeability on effective stress by comparing the pressure change $\kappa q_0 T_k/(\beta\phi)$ to the stress sensitivity parameter σ^*. The pressure change is the fluid transported by steady flow at rate q_0 over timescale T_k, spread over the length scale κ^{-1}, divided by the specific storage $\beta\phi$. J is the ratio of the characteristic slip distance for permeability evolution ($V_0 T_k$) to the state evolution distance d_c. P, R, M, J are always positive (for $\kappa > 0$). The sign of Q is the same as the sign of Δk, which in most cases is positive.

3.2 No state evolution limit

It is useful to neglect the state evolution effect as it separates the classical frictional instability that occurs for velocity-weakening friction. There are several ways to neglect the state evolution effects from (14). The first is to simply set $b = 0$, which yields

$$(PS + 1)(S + 1)(S + R + iM) + iPQS = 0. \tag{20}$$

Even with non-zero b, state evolution is essentially negligible if J is either very small or very large. By taking the limit of $J \to 0$, we again obtain equation (20) because the permeability evolution time, and hence the fault valve instability, occurs over time scales much shorter than required for state evolution. The frictional response is the direct effect in this limit. For $J \gg 1$, state evolution is much faster than permeability evolution and friction is effectively always in steady state. This is similar to the previous limit but with a replaced with $a - b$ (i.e., P and Q are replaced by $Pa/(a - b)$ and $Q(a -$

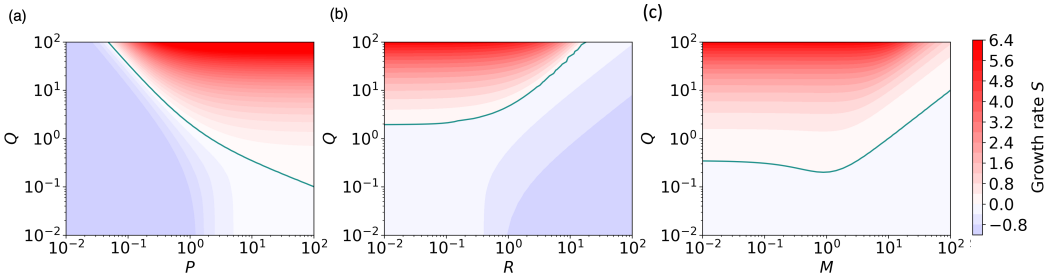

Figure 2. The maximum growth rate Re(S) calculated from equation (20). (a) P-Q space with $R = 1$ and $M = 0$. (b) R-Q space with $P = 1$ and $M = 0$. (c) M-Q space with $P = 1, R = 0.01$.

$b)/a$, respectively). This can be seen from the $J \to \infty$ limit of equation (14) (see Appendix).

Equation (20) has four complex solutions and we focus on the solution with the greatest real part as it dominates the system behavior. We plot max(Re(S)) for various dimensionless parameters in Figure 2. Part of the parameter space exhibits unstable behavior, which we call the fault-valve instability. This instability is fundamentally different from the classical frictional instability arising from velocity-weakening friction, since we have already neglected state evolution and assumed $a > 0$. The system is most unstable for large values of Q and P. The diffusion parameter R has a stabilizing effect. Finally, the dependence on M is non-monotonic. For $M \ll 1$, the effective stress dependence of permeability is negligible. For M larger than unity, this process acts in a stabilizing manner. However, for $M \sim 1$, this process slightly enhances the instability.

3.3 Minimal conditions for the fault-valve instability

To find the minimal conditions for instability, we further neglect the effect of diffusion ($R = 0$) and the effective stress dependence of permeability ($M = 0$), as they are not essential for instability. Equation (20) simplifies to

$$(PS + 1)(S + 1) + iPQ = 0. \tag{21}$$

This model accounts for fault valving (i.e., permeability evolution that leads to reductions in frictional strength through changes in fluid pressure), the direct effect, and elasticity.

Next we eliminate each of these processes one by one to identify which are essential for instability. Recall that P is the ratio of the direct effect to elasticity, and Q is the ratio of fault valving to the direct effect. Thus, PQ is the ratio of fault valving to elasticity, which is independent of the direct effect. If we neglect the direct effect in (21) by taking $P \to 0$ while keeping PQ finite, then sliding occurs at constant friction coefficient and we have retained only elasticity and fault valving. The solution is $S = -1 - iPQ$. Similarly, if we instead neglect permeability evolution in (21) (by taking $T_k \to 0$ so that permeability depends only on slip rate), then the solution is $S = -1/P - iQ$. (Note that all terms are proportional to T_k, which then cancels out). Both solutions in these extreme limits are always stable. It follows that the frictional direct effect (with $a > 0$), permeability evolution ($T_k > 0$), and non-zero Q are required to generate the fault valve instability.

On the other hand, if we neglect elasticity in (21) by taking $P \to \infty$, we obtain the minimal condition for the fault-valve instability. The characteristic equation is

$$S^2 + S + iQ = 0. \tag{22}$$

The two solutions depend only on a single parameter: Q. Figure 3 shows the solutions as a function of Q. There is an unstable mode and a stable mode. The unstable mode has a negative imaginary part, meaning the instability propagates in the direction of fluid flow (for $\Delta k > 0$). The other solution is always stable, and propagates in the opposite direction.

We examine the asymptotics for small and large Q. In the case of positive Δk, the solutions for $Q \ll 1$ are

$$S = -\frac{1}{2} \pm \left(\frac{1}{2} + Q^2 - iQ \right). \tag{23}$$

and the solutions for $Q \gg 1$ are

$$S = \pm \left(\sqrt{\frac{Q}{2}} - i\sqrt{\frac{Q}{2}} \right). \tag{24}$$

Therefore, the growth rate of one mode is always positive for all non-zero Q.

It is useful to discuss the instability in terms of wavelength. Equation (15) shows that we can write $Q = \kappa L_v$, where

$$L_v = \frac{f_0 q_0 \Delta k T_k}{k_0 \beta \phi a \sigma_0} \tag{25}$$

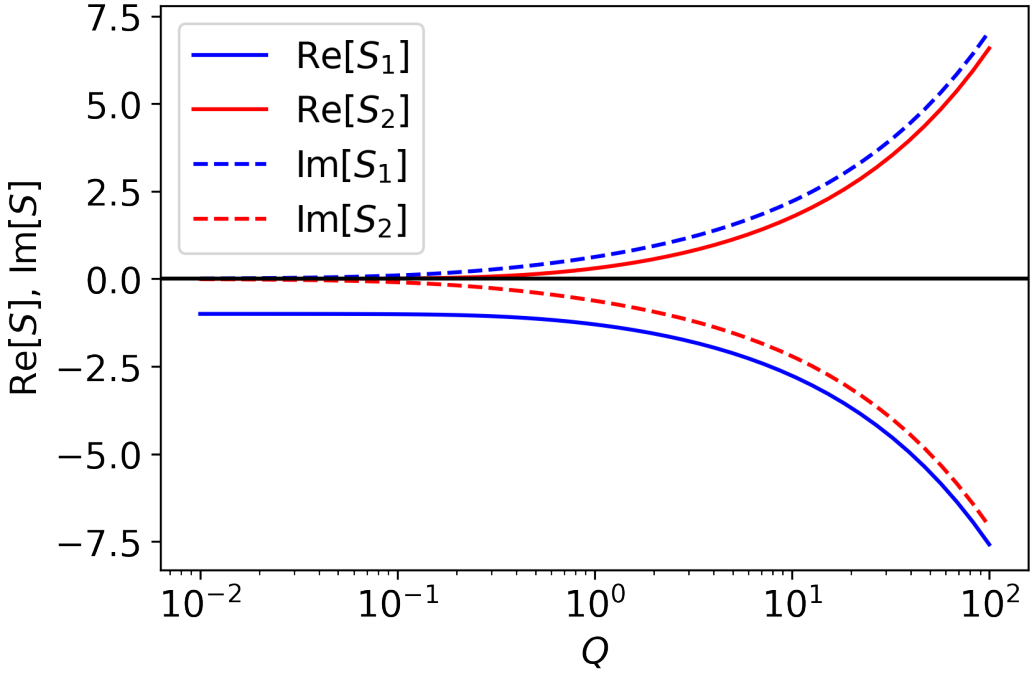

Figure 3. Two solutions of the characteristic equation (22). S_1 is the stable mode propagating in the opposite direction of fluid flow and S_2 is the unstable mode propagating in the direction of fluid flow.

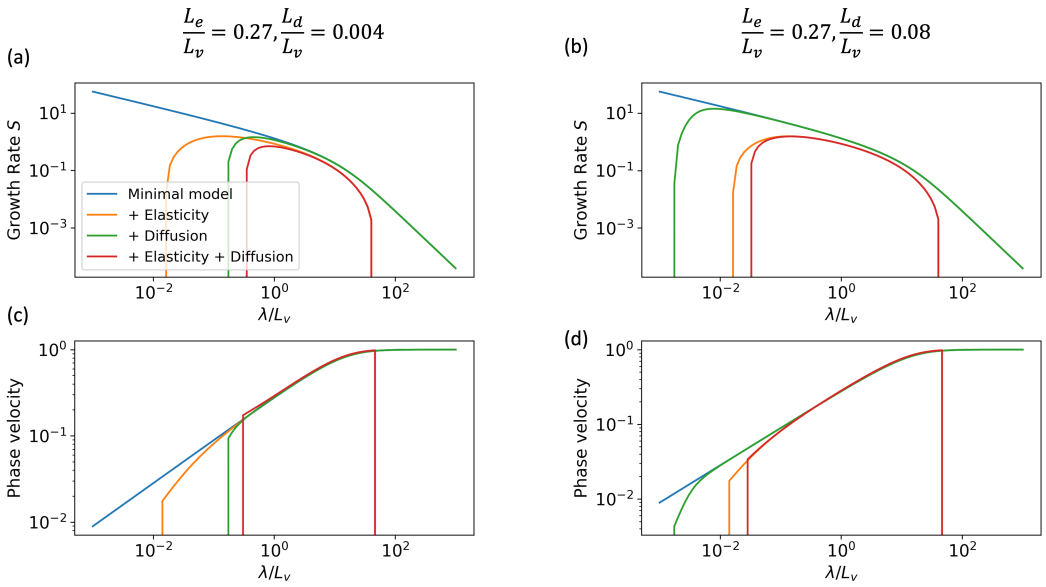

Figure 4. Growth rate Re(S) and phase velocity V_{phase} (normalized by $\frac{f_0 q_0 \Delta k}{k_0 \beta \phi a \sigma_0}$) as a function of wavelength λ. Parameters are $k_0 = 10^{-15}$ m^2, $\Delta k = 10^{-15}$ m^2, $a = 0.01$, $\sigma_0 = 10$ MPa, $\mu^* = 32.04$ GPa, $T_k = 10^7$ s, $\beta = 10^{-9}$ Pa^{-1}, $\phi = 0.01$. Neglecting elasticity corresponds to setting $P^{-1} = 0$ and neglecting diffusion corresponds to setting $R = 0$. Both elasticity and diffusion are neglected in the minimal model.

is the fault valve length scale. The asymptotic growth rate in the two limits above is

$$\mathrm{Re(s)} = \begin{cases} \left(\frac{f_0 q_0 \Delta k \kappa}{2 k_0 \beta \phi a \sigma_0 T_k}\right)^{\frac{1}{2}}, & \kappa \gg L_v^{-1}, \\ \frac{\kappa f_0 q_0 \Delta k}{k_0 \beta \phi a \sigma_0}, & \kappa \ll L_v^{-1}. \end{cases} \tag{26}$$

As can be seen in Figure 4, growth rate has a linear dependence on wavelength at short wavelengths, and square root dependence at long wavelengths.

Next we examine phase velocity, which is given by $V_{phase} = -\mathrm{Im(s)}/\kappa$ with asymptotic behavior

$$V_{phase} = \begin{cases} \left(\frac{f_0 q_0 \Delta k}{2 k_0 \beta \phi a \sigma_0 \kappa T_k}\right)^{\frac{1}{2}}, & \kappa \gg L_v^{-1}, \\ \frac{f_0 q_0 \Delta k}{k_0 \beta \phi a \sigma_0}, & \kappa \ll L_v^{-1}. \end{cases} \tag{27}$$

The phase velocity is asymptotically constant for large wavelengths.

If Δk is negative, the propagation direction of the modes are reversed while keeping the same growth rate. This is because q_0 and Δk appear only in the dimensionless parameter Q, and only as the product $q_0 \Delta k$.

3.4 Stabilizing effects of elasticity and diffusion

We have seen in the minimal model that all wavelengths are unstable and shorter wavelengths have higher growth rates. Now we add elasticity and diffusion, which have a stabilizing influence and lead to growth rate being maximized at a nonzero wavelength.

As with L_v, we introduce two additional length scales. First, we rewrite $P = (2\kappa L_e)^{-1}$, where

$$L_e = \frac{\mu^* V_0 T_k}{a\sigma_0}, \tag{28}$$

is the characteristic length scale of elasticity. The other is related to diffusion. We write $R = (\kappa L_d)^2$, where

$$L_d = \sqrt{c_0 T_k} \tag{29}$$

is the hydraulic diffusion length. The relationship between L_v, L_e, L_d controls the wavelength dependence of the fault valve instability.

First we add elasticity while neglecting diffusion. The system is stable for all wavelengths when $L_e < L_v$. When $L_v < L_e$, then adding elasticity decreases the growth rate for all wavelengths, relative to the minimal model without elasticity, and stabilizes sufficiently short and long wavelengths. Between the two cutoff wavelengths that delimit this stability boundary, the growth rate is positive. We have analytical expressions for these neutrally stable wavelengths by solving equation (20), assuming S to be purely imaginary, which leads to

$$\lambda_e = \frac{\pi L_e^3}{(L_v \pm \sqrt{L_v^2 - L_e^2})^2}. \tag{30}$$

Next we add diffusion while neglecting elasticity. The system is stable for all wavelengths when $L_v < L_d$. When $L_d < L_v$, then diffusion stabilizes only short wavelengths. The growth rate is positive for $\lambda > \lambda_d$, where

$$\lambda_d = 2\pi\sqrt{\frac{L_d^3}{L_v - L_d}}, \tag{31}$$

which is confirmed by Figure 4.

Finally, we add both elasticity and diffusion. We consider two cases: $\lambda_e < \lambda_d$ and $\lambda_d < \lambda_e$ by changing the effective normal stress σ_0. The upper limit of unstable wavelengths is controlled by elasticity, since diffusion stabilizes only short wavelengths. The lower limit can be controlled by either elasticity or diffusion.

The preferred wavelength (i.e., the one with maximum growth rate) is close to the minimum wavelength having a positive growth rate. The non-monotonic nature of the growth rate over wavelengths, in particular stability of long wavelengths, suggests that unstable slip takes the form of a slip pulse rather than a crack, as in Heimisson et al. (2019). Adding elasticity and/or diffusion does not significantly change the phase velocity (Figure 4). Thus, the maximum propagation speed of the instability is bounded by equation (27).

3.5 State evolution effects

To close this section, we return to the full model (including state evolution) to connect the fault valve model with the classical frictional instability. Figure 5 shows the growth rate as a function of $a - b$ and wavelength. Two values of J are used by changing d_c. In the case of $J \ll 1$, state evolves much slower than permeability and a controls the instability as seen in section 3.2. In the case of $J \gg 1$, the behavior depends on $a-b$. The growth rate increases monotonically with λ for negative $a-b$ (velocity-weakening friction). The minimum wavelength for instability is the critical wavelength given by $\lambda_{rsf} = \frac{\pi \mu d_c}{(b-a)\sigma_e}$ (Rice et al., 2001). That is, fault valving processes are of secondary importance and the instability is effectively the usual frictional instability. For positive $a-b$ (velocity-strengthening friction), the fault valve instability produces unstable wavelengths with a preferred wavelength that depends on $a - b$.

4 Idealized Numerical Simulations

We have seen that velocity-strengthening faults can be unstable through the fault valve mechanism, but linear stability analysis alone does not reveal how the instability develops away from the steady state. Numerical simulations are required to explore the dynamics of unstable slip. We use the specific permeability evolution law in equations (3) and (5).

4.1 Numerical Method

We use the quasi-dynamic boundary element method to calculate the elastic stress transfer on the fault (Rice, 1993), which is accelerated using H-matrices as detailed in S. Ozawa et al. (2023). We use the SBP-SAT finite difference method (Mattsson, 2012)

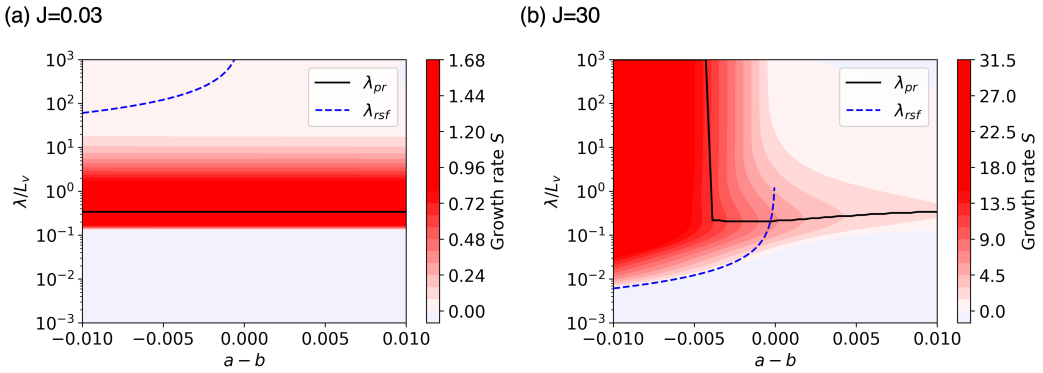

Figure 5. The effect of state evolution. (a) $J = 0.03$ and (b) $J = 30$. The dashed line is the critical wavelength $\lambda_c = \frac{\pi\mu d_c}{(b-a)\sigma_e}$ for a velocity-weakening fault with constant effective normal stress (Rice et al., 2001). Because $a = 0.010$, the right edge of the horizontal axis corresponds to pure velocity-strengthening friction. The solid line is the preferred wavelength. Note that λ_{pr} jumps to infinity for negative $a - b$ in (b). We used $d_c = 10^{-6}$ m, and other parameters are identical to Figure 4.

to solve the fluid pressure diffusion equation (1) with variable coefficients. The diffusion equation is stiff and must be solved by an implicit method to avoid numerical instability when long time steps are used. We use an operator splitting scheme similar to Zhu et al. (2020). We use an explicit fifth order Runge-Kutta method for the time stepping of τ, ψ and k^*. The time step is adjusted with the relative error computed from the difference between the fifth and fourth order solutions (Press et al., 2002). We then solve equation (1) using the backward Euler method. We solve the sparse linear equation by the conjugate gradient method. Fixed point iteration is used to find a consistent solution between k^* and σ_e in equation (3). The accuracy of this method is first order in time due to the use of operator splitting. We verified our code on the SEAS benchmark problem BP6 (https://strike.scec.org/cvws/seas/index.html) for the special case of uniform diffusion coefficients.

To enhance the comparison with the linear stability analysis, we first consider the case of homogeneous parameters in an elastic whole space and neglect gravity. The fault is loaded by constant creep at $V = V_0$ outside the computational domain by the backslip approach. The fluid pressures at both ends of the fault are set to values consistent with the steady-state flow rate q_0 and permeability k_0, i.e., $p_r - p_l = L_f \eta q_0 / k_0$, where

L_f is the fault length. We also tested the Neumann boundary condition (fixed flow rate q_0 at the boundary) and got similar results except near the boundary. We set the total normal stress so that the background effective normal stress is uniform (i.e., $\sigma(x) = \sigma_0 + p(x)$). We start a simulation by setting the initial slip rate 1% higher than the loading rate.

4.2 Example of spatiotemporal slip pattern

We first show a representative result with velocity-strengthening friction with no state evolution using the same parameters as Figure 4a. Figure 6 shows the space-time plots for slip rate, fluid pressure, permeability, and flow rate. We present our results in a non-dimensional form. There are aseismic slip events that span the entire fault domain. They take the form of a slip pulse rather than a crack, since only the tip of the rupture is sliding at any given time. The pulses propagate in the direction of the background fluid flow. The peak slip rate is about 20 times faster than the loading rate, much lower than the seismic slip rate that is limited by radiation damping. The propagation velocity of the slip pulse is nearly equal to the phase velocity for λ_{pr} derived from the linear stability analysis.

All variables are synchronized. When the slip front arrives, sudden fluid pressurization occurs as a result of the increase in fluid flow. Weakening due to fluid pressurization, combined with the elastic stress concentration, accelerates slip at the pulse front (Figure 6a). However, slip acceleration increases permeability and hence fluid outflow (Figures 6c-d), limiting weakening by pressurization. Note that the weakening is driven by fluid pressurization alone, as there is no state evolution in this case and friction is velocity-strengthening.

4.3 Comparison with linear stability analysis

We perform a parameter space study for $a-b$ and Q and plot the maximum slip rate V_{max} in Figure 7. Q is varied by changing q_0 with the other parameters fixed. $V_{max} = V_0$ indicates stable sliding and higher values indicate the occurrence of stick-slip. We see that the critical Q at the transition from stable sliding to stick-slip is quantitatively consistent with the linear stability analysis. In the unstable part of the positive $a-b$ do-

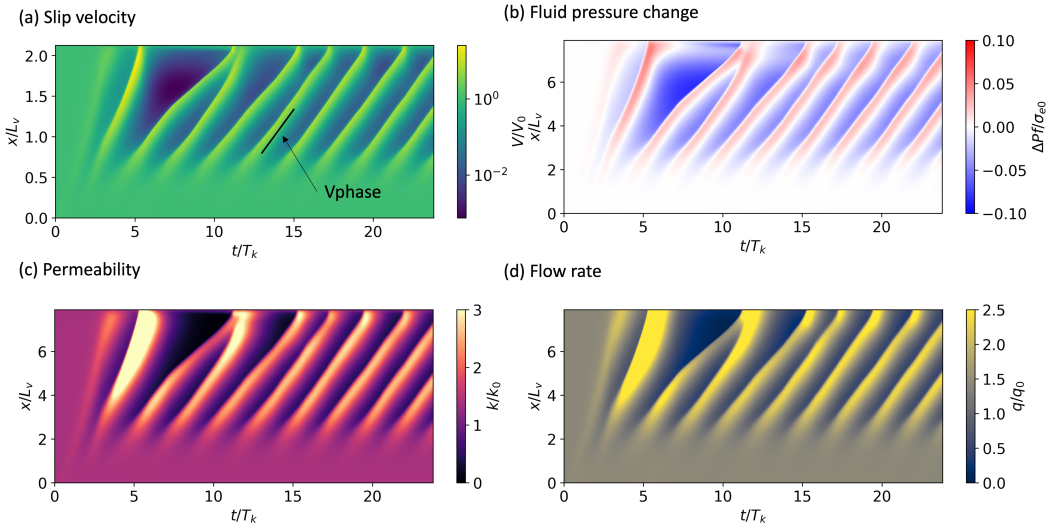

Figure 6. Space-time plot of slip rate, fluid pressure, permeability, flow rate for the idealized model. Parameters are shown in Table 1. The phase velocity for the preferred wavelength calculated from the linear stability analysis is shown in the slope in (a).

main, the maximum slip rate increases slightly with flow rate, although it is still much slower than typical slip rates during earthquakes (∼1 m/s).

As a further comparison with the linear stability analysis, we vary the length of the fault using the same set of parameters (Figure 8). As expected, $W > \lambda_{min}$ is required to generate unstable slip. When W and λ_{pr} are of the same order, there are periodic slow slip events. When $W \gg \lambda_{pr}$, nonlinear effects are prominent. There is coalescence of two slip pulses during their propagation, since the propagation velocity is not constant and typically much faster than predicted by the linear stability analysis. Consequently, the recurrence interval of slip at a given point on the fault is much longer for the low pressure (fluid outlet) side of the fault.

5 Subduction zone simulations

5.1 Model

We have shown the emergence of unstable aseismic slip due to the fault valve instability. One question is whether the parameters in real subduction zones are in a range that would produce the fault valve instability. In addition, the assumption of spatially

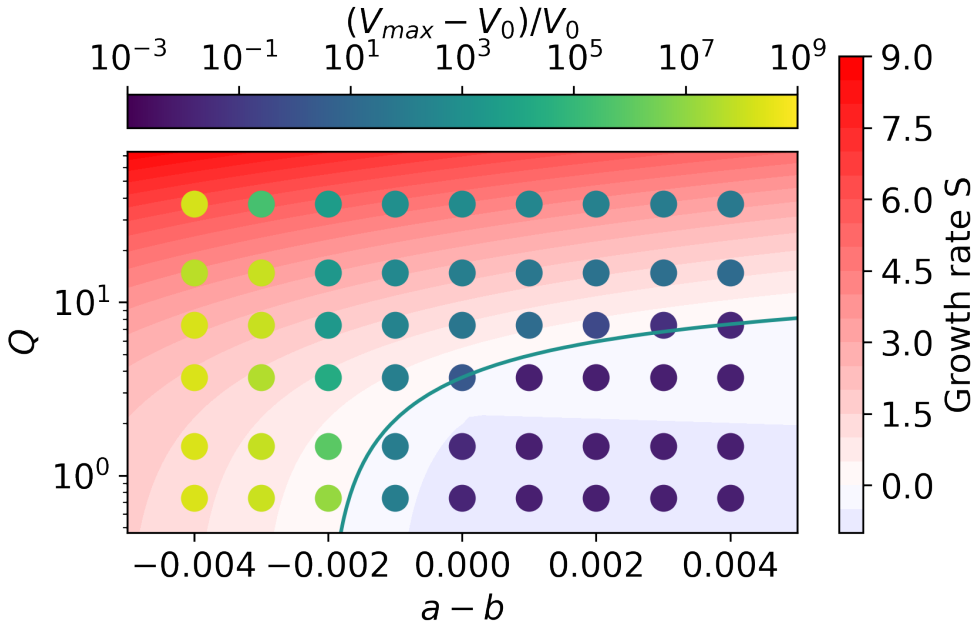

Figure 7. Comparison of numerical simulations and linear stability analysis. The color of each circle indicates the peak slip rate normalized by the loading rate. The background blue to red colors show the maximum growth rate computed from the linear stability analysis, and the solid line indicates the stability boundary. In numerical simulations, Q is varied by changing q_0 with other parameters fixed.

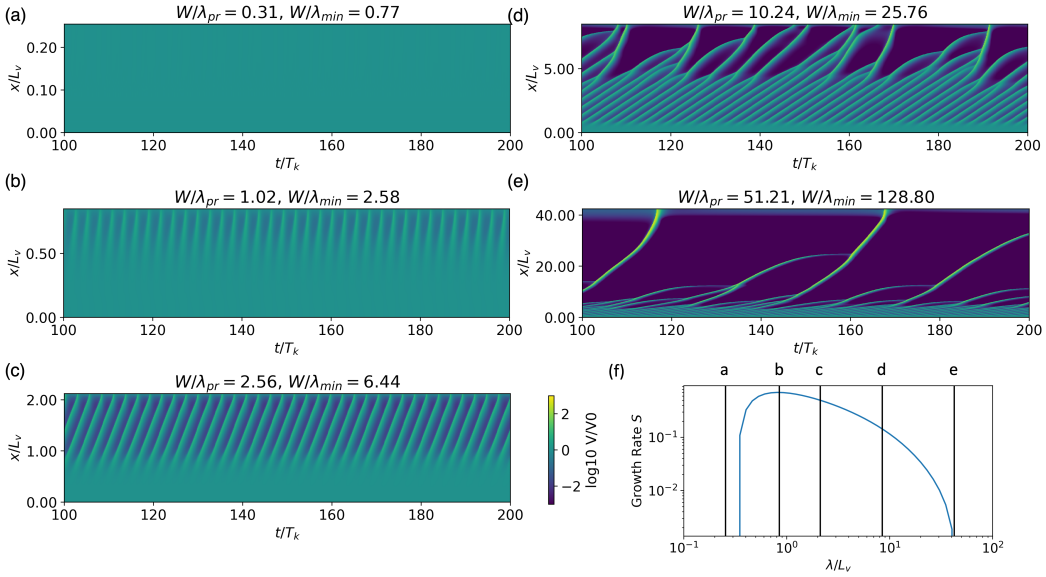

Figure 8. (a-e) Space-time plots of slip rate for different fault lengths. (f) Growth rate from linear stability analysis, with vertical black lines marking the fault length value corresponding to panels a-e. Stable creep occurs when $\lambda < \lambda_{min}$ and complex behavior with multiple slip pulses occurs when $\lambda \gg \lambda_{pr}$.

uniform parameters is not valid for real tectonic settings. In this section, we perform earthquake cycle simulations on a megathrust.

We consider depth-dependent physical properties such as $a-b$ and permeability. The fault is 200 km long, embedded in an elastic half-space, and the dip angle is 15°. We consider the effect of the free surface using the elastostatic Green function (Segall, 2010), but changes in fault normal stress are neglected when computing fault strength for simplicity. The normal stress change would only be significant in the shallowest region, and additional processes are likely important there that are not included in the model (e.g., inertial effects during rupture propagation, inelastic yielding, and a modified elastic response from compliant sediments). We present four models here, namely the reference model (Model A) and three models that change only one component from the reference (Models B-D). These are the frictional transition depth (Model B), the permeability (Model C), and the fluid sink (Model D).

The friction parameter $a - b$ transitions from negative to positive (i.e., velocity-weakening to velocity-strengthening) at a certain depth, which sets the maximum depth

Table 1. Parameters for the simulation

Symbol	Description	Section 4	Section 5
μ^*	Generalized shear modulus	32.04 GPa	32.04 GPa
ρ_r	Density of rock		2600 kg/m^3
ρ_f	Density of fluid		1000 kg/m^3
g	Gravity acceleration		9.8 m/s^2
d_c	State evolution distance	1 mm	5 mm
V_0	Loading velocity	10^{-9} m/s	10^{-9} m/s
f_0	Reference friction coefficient	0.6	0.6
a	Direct effect	0.01	Figure 9
b	Evolution effect	Variable	Figure 9
L	Permeability evolution distance	1 m	5 mm
k_{max}	Maximum permeability	10^{-14} m^2	10^{-12} m^2
k_{min}	Maximum permeability	10^{-18} m^2	10^{-18} m^2
ϕ	Porosity	0.1	0.1
σ^*	Effective stress dependence of permeability		20 MPa
σ_0	Background effective normal stress	10 MPa	Figure 10
η	Fluid viscosity	10^{-4} Pa s	10^{-4} Pa s
β	Sum of the pore and fluid compressibility	10^{-9} Pa^{-1}	10^{-9} Pa^{-1}
q_0	Background flow rate	2×10^{-8} m/s	Figure 9
T	Healing time	10^7 s	Figure 9
T_0	Healing time for infinite temperature		1.0 s
Q_a	Activation energy		83 kJ^{-1} mol^{-1}
R_g	Gas constant		8.3 J mol^{-1} K^{-1}

583 extent of megathrust ruptures. The transition depth is 24 km for the reference model
584 and 32 km for Model B (Figure 9d).

585 We assume that permeability healing timescale has an Arrhenius-type dependence
586 on temperature:

$$T = T_0 \exp(Q_a / R_g \Theta), \tag{32}$$

587

where T_0 is the reference healing time, Q_a is the activation energy, Θ is the absolute temperature, and R_g is the gas constant. We use values that fit well with the results of laboratory experiments measuring permeability evolution, such as Giger et al. (2007) and Morrow et al. (2001). Arrhenius-type fitting predicts very long T (greater than 1000 years) for low temperature (Figure 9a), although the room temperature slide-hold-slide test in Im et al. (2019) showed an order of magnitude reduction in fracture permeability over a few hours. Therefore, the healing time at lower temperatures may be overestimated because temperature-insensitive healing mechanisms are neglected in our model. To relate depth to healing time T, we assume a linear geothermal gradient as $\Theta(z) = 300 + 12z$ K for z in km along the plate interface, which is motivated by the estimate in the Cascadia subduction zone (e.g., Van Keken et al. (2011)). However, we do not attempt to tune our model to reproduce slow slip events in the region. The distribution of T and T_k is shown in Figure 9b.

The model of Zhu et al. (2020) assumes that the fluid source is below the model domain, whereas we consider the fluid source within the model domain. In subduction zones, dehydration reactions occur over a wide depth range from the seismogenic zone to a few hundred kilometers depth (Hacker et al., 2003; C. B. Condit et al., 2020), suggesting that the maximum fluid production corresponds at least approximately to the depth of slow slip events. Calculation of the depth dependence of fluid flow rate, taking into account the dehydration reaction expected from the P-T path of subducting rocks, would be important for future work.

Fluids can flow into the upper plate if it is permeable. The permeability of the upper plate may vary significantly along dip due to changes in lithology. For example, Hyndman et al. (2015) proposed that the serpentinized mantle wedge corner has lower permeability and forces the fluid to flow along the plate interface. After passing the mantle wedge corner, the fluids can flow into the overriding plate.

For all models we assume a fluid source at 40 km depth. In addition, we add a fluid sink at 31 km depth following Hyndman's conceptual ideas in model D. This results in the background flow distribution shown in Figure 9c. Other parameters are given in Table 1.

5.2 Steady state and linear stability

We obtain the depth profile of the effective normal stress, permeability at steady state, as in previous studies (Rice, 1992; Zhu et al., 2020; Yang & Dunham, 2023; Kaneki & Noda, 2023). The effective stress profile can be obtained by integrating

$$\frac{d\sigma_e}{dx} = (\rho_r - \rho_f) g \sin\theta - \frac{\eta q(x)}{k^*(x)} e^{\sigma_e/\sigma^*}, \tag{33}$$

where x is the along-dip distance, ρ_r is the density of the rock, and θ is the dip angle. The boundary condition at $x = 0$ is $p = 0$. The effective stress and permeability are determined in a self-consistent manner with the other hydraulic properties.

The calculated steady state σ_e and k for the four models are shown in Figure 9e-f. Increasing temperatures with depth decrease k and σ_e, since healing of permeability is more efficient. This feature was not observed for the depth-independent healing time (Zhu et al., 2020). The effective stress reaches $\sigma_e \sim 100$ MPa in the middle of the seismogenic zone in this setting due to our choice of higher permeability in Model A, but the value is lower for Model C using 20 times lower k_{max} (note that k_{max} is the permeability at the trench). The permeability is similar between Models A and C except at shallow depths, despite the large difference in effective normal stress at deeper depths. For a fluid sink at the mantle wedge corner (Model D), the effective normal stress is lower than the surrounding due to high flow rates. Frictional properties do not affect either the effective normal stress or the permeability at steady state (Model B).

We also compute the growth rate Re(s) using linear stability analysis for a range of wavelengths (Figure 10). Both velocity-weakening and velocity-strengthening regions are unstable. The velocity-weakening region is the classical frictional instability with longer wavelengths being most unstable, while the velocity-strengthening region exhibits the fault-valve instability with the maximum growth rate around $\lambda \sim 20$ km. In Model C, the unstable wavelength is longer due to the small effective normal stress. In Model D, the growth rate is negative in the up-dip region of the mantle wedge corner, implying that slow slip events do not occur at these depths.

5.3 Simulation Results

We perform earthquake sequence simulations for the four model settings. Figure 11 shows the space-time plot of slip rate as well as the origin times and hypocenter lo-

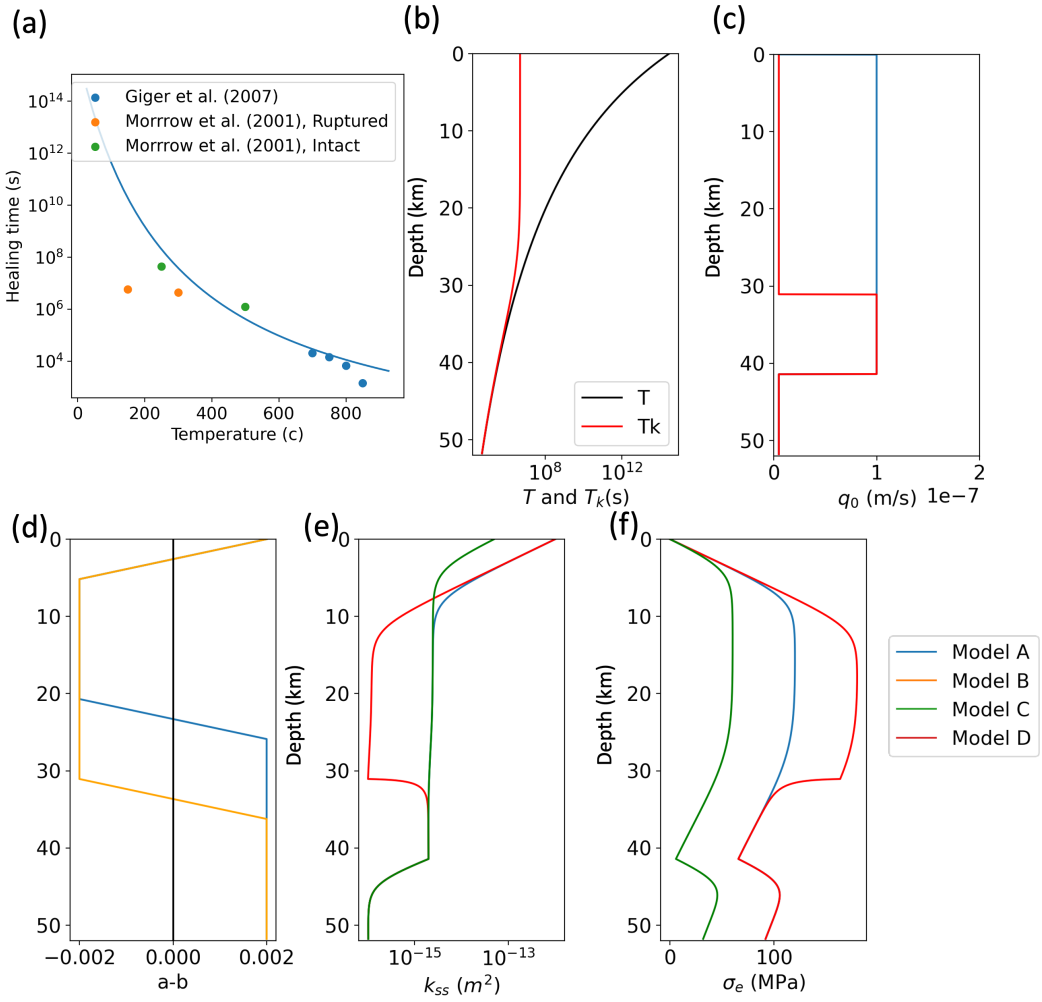

Figure 9. Subduction zone models. (a) Temperature dependence of the healing time T given by equation (32) with data from lab experiments. Depth profile of (b) T and T_k, (c) q, (d) $a - b$. The solution obtained by integrating equation (33) is shown for (e) k_{ss} and (f) σ_{ss}.

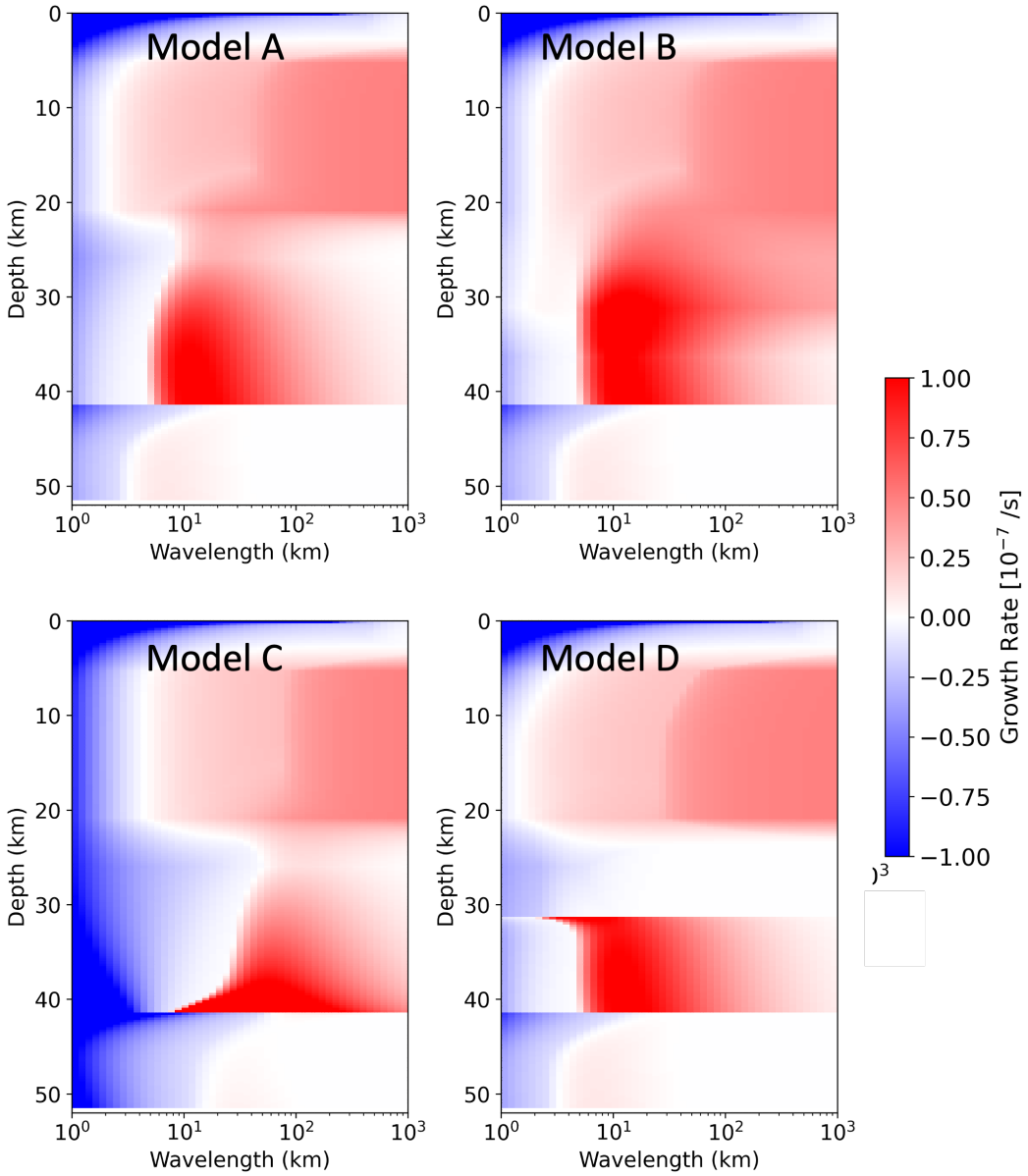

Figure 10. The maximum growth rate Re(s) of instability from the linear stability analysis.

cations from a synthetic earthquake catalog. An earthquake is defined when maximum slip rate is greater than $V_{th} = 10^{-2}$ m/s and its hypocenter is the location where the slip rate first exceeds V_{th}. For Model A, Figure 12 shows time series for slip rate and fluid pressure at four depths before and after a megathrust earthquake.

We start with Model A as a reference. Many small earthquakes occur throughout the earthquake cycle in the seismogenic zone (between 5 km and 24 km depth) with most hypocenters between 10 km and 20 km depth. Numerous slow slip events with peak slip rates of 10^{-8} to 10^{-7} m/s occur at a depth range between 15 km and 35 km. The slow slip events begin in the velocity-strengthening region and propagate up-dip into the velocity-weakening region. Their propagation speed slows down when moving up-dip. This was not seen in the previous model using spatially uniform healing time (Zhu et al., 2020). While linear stability analysis predicts everywhere up-dip of the fluid source (42 km depth or 160 km along-dip) is unstable, the slow slip events initiate about 20 km up-dip of the fluid source. The stable slip near the fluid source is similar to what we have seen in Figure 8 and probably occurs because short wavelengths are stable and the fault length needs to be sufficiently long to create an instability. Also, the recurrence interval of slow slip events becomes longer when moving up-dip: a few months at 36 km depth and a few years at 26 km depth (Figure 12c-d). There are many coalescences of two slow slip events as propagating up-dip. The recurrence interval of slow slip events in Cascadia and Nankai also decreases with depth (Wech & Creager, 2011; Obara, 2010), although other models exist which explain the depth dependence of the recurrence interval by assuming a systematic decrease of effective stress with depth (Luo & Liu, 2021).

Unlike the uniform-T model which shows a gradual increase of the up-dip extent of slow slip late in the cycle (Zhu et al., 2020), the pattern of slow slip events as well as earthquakes in our model does not show significant changes over a seismic cycle. Small earthquakes at the base of the seismogenic zone migrate up-dip before a megathrust earthquake (Figrue 11a). However, up-dip migration of seismicity frequently occurs and does not result in a megathrust earthquake in most cases.

In the source region of slow slip, the negative correlation between slip rate and effective normal stress is very clear (Figure 12c-d). In the seismogenic zone (Figure 12 a-b), the correlation is not clear as pore pressure is controlled by fluid input from deeper

regions, which is in turn controlled by the slow slip events. The local variation in pore pressure in the slow slip region over a slow slip cycle is up to 10 MPa.

In Model B (deeper transition depth of friction), slow slip events are observed at approximately the same depths as in Model A, although the duration of slip at a given location on the fault is shorter. There are sometimes regular earthquakes in the slow slip region as friction is velocity-weakening. In Model C (low k_{max}), we still observe slow slip events at mostly similar depths compared to the reference Model A. The slow slip events show shorter recurrence intervals near the fluid source as predicted from the linear stability analysis (Figure 10).

In Model D (fluid sink at the mantle wedge corner), slow slip events are confined in the high flow rate region between the fluid source and sink. Up-dip of the mantle wedge corner, the flow rate is too small and the fault valve instability is disabled, as we observe from the linear stability analysis (Figure 10). There are many small earthquakes immediately before an earthquake, but the seismicity is less active during the interseismic period than in other models. In addition, Model D shows longer and larger postseismic slip down-dip of the seismogenic zone.

6 Discussion

6.1 Comparison with other models for slow slip

There is a large difference in the recurrence interval between megathrust earthquakes and slow slip in our Model A (Figure 11), even with relatively uniform effective normal stress. These are because earthquakes and slow slip events are the manifestation of two different mechanisms of instability. This contrasts with the rate-and-state model with constant (in time) fluid pressure (Liu & Rice, 2007; Matsuzawa et al., 2013; Barbot, 2019; Li & Liu, 2016), in which the slow slip events are the same instability as ordinary earthquakes, but near the stability boundary. The classical rate-and-state model requires very low (few MPa) effective normal stress in the slow slip region, much smaller than the tens to hundreds of MPa effective stress in the seismogenic zone, in order to produce the short recurrence interval of slow slip as compared to the megathrust earthquakes. These models impose the required effective stress distribution through a spatially compact region of extremely high pore pressure, which drops discontinuously or at least with an extreme gradient to a much smaller value in the seismogenic zone. These models provide little

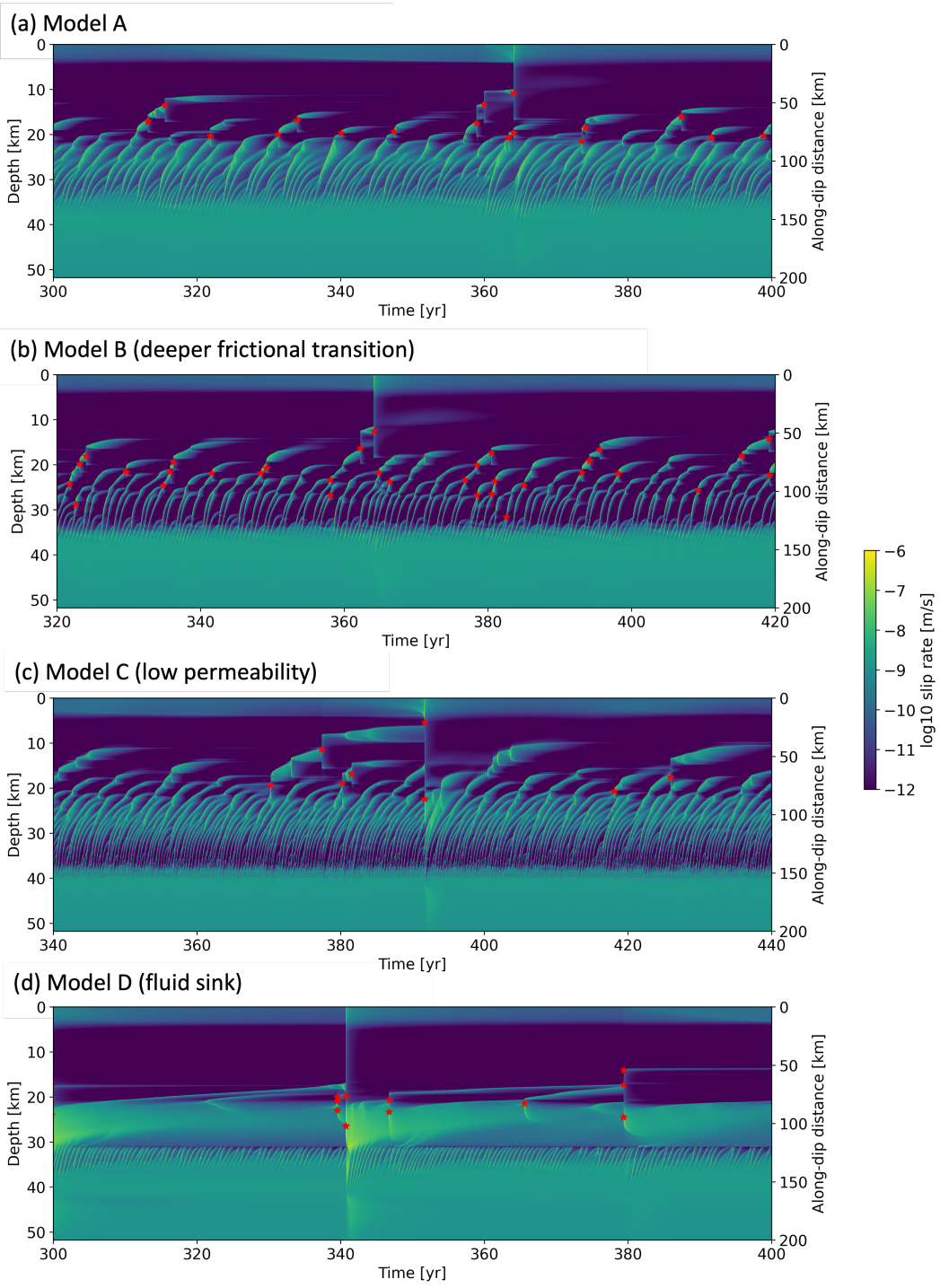

Figure 11. Space-time plots of slip rate for the megathrust simulations. (a) Model A (reference model) (b) Model B (deeper friction transition) (c) Model C (low permeability k_{max}). (d) Model D (fluid sink at the mantle wedge corner). Red stars indicate the hypocenters of earthquakes from the synthetic catalog.

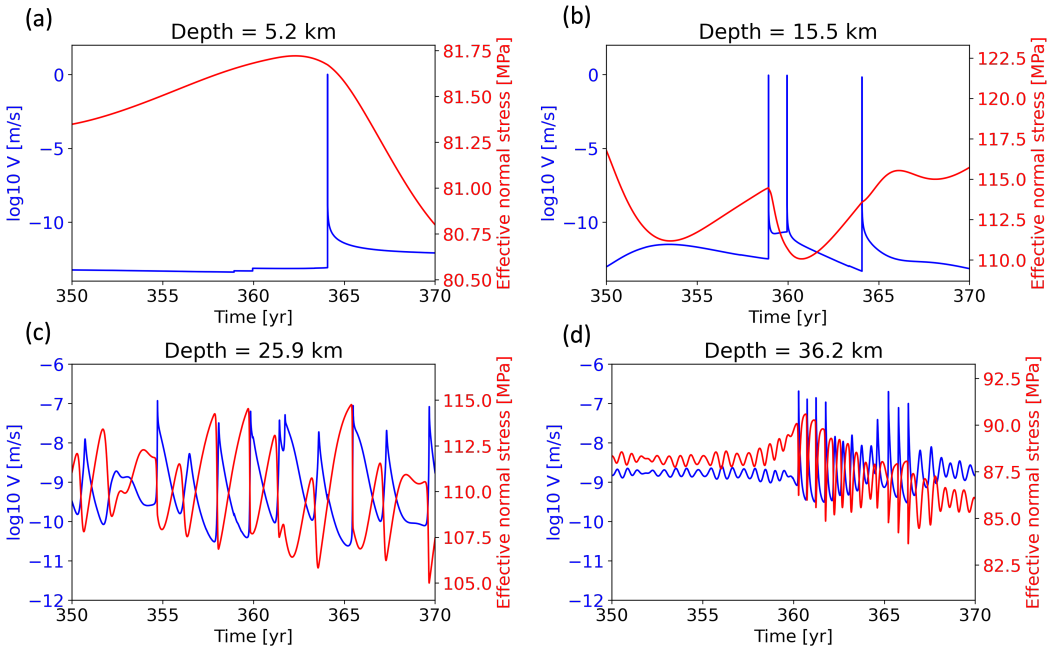

Figure 12. Time series of slip rate and effective normal stress at four locations for Model A. Note that full rupture of the seismogenic zone occurs at $t = 364$ years.

justification for how such extreme pressure gradients can be maintained without driving significant outflow, and hence depressurization, of the slow slip region. In our calculation of steady-state effective normal stresses, we show that locally high flow rate along the fault, and fluid loss from the megathrust above the slow slip region, is needed to produce an effective stress distribution similar to that assumed in Liu and Rice (2007) (Model D).

Several models incorporate the coupling between fluid pressure and slip and simulate the evolution of fluid pressure (Aochi et al., 2014; Dal Zilio & Gerya, 2022; Yamashita, 2013; Chen, 2023; Perez-Silva et al., 2023; Noda & Lapusta, 2010; Marguin & Simpson, 2023; Petrini et al., 2020; Heimisson et al., 2021; Dublanchet & De Barros, 2021; Hooker & Fisher, 2021). The way of inclusion is not unique and depends on the assumed process(es). A common way to account for fluids in modeling slow slip events is slip-induced dilatancy, which is neglected in our model. The fluid pressure suction due to slip-induced dilatancy stabilizes the system and expands the range of effective normal stresses that generate slow slip (Segall et al., 2010; Liu & Rubin, 2010; Sakamoto & Tanaka, 2022). However, the model still requires velocity-weakening friction. Recently, Yang and Dun-

ham (2023) added creep compaction of pores to dilatancy models. Their model produces slow slip events in the bottom portion and down-dip of the seismogenic zone. Their slow slip events are caused by the combination of low effective normal stress due to viscous compaction and the stabilizing effect of dilatancy on slip acceleration. They assumed velocity-weakening friction in the region of slow slip. Perfettini and Molinari (2023) studied the combined effects of viscoelasticity and dilatancy on the generation of slow slip events around the brittle-ductile transition depth.

Perez-Silva et al. (2023) modeled slow slip events on velocity-strengthening faults in 3D, which occur in response to periodically imposed fluid pressure changes, and came to a similar conclusion that high permeability (or hydraulic diffusivity) is required to explain the observed migration rate of slow slip. Our model also produces slow slip events with velocity-strengthening friction, but the fluid pressure pulses arise spontaneously in our model as part of the internal dynamics of the system.

The fault-valve mechanism of slow slip is similar to the poroelastic bimaterial model of Heimisson et al. (2019), despite the conceptually different setting and governing equations. In their model, fluid pressure is coupled to slip through the undrained poroelastic response. When slip is localized on either side of the permeable fault core, symmetry breaking occurs. The direction of migration is determined by the location of the slip within the fault core. Their model better explains the existence of both up-dip and down-dip migration of slow slip, which is what is observed in nature (Obara et al., 2012). In contrast, the fault valve instability produces along-flow and hence up-dip migration only (assuming permeability increases with slip rate). Ide (2012) shows that up-dip migration of tremor is more common in some subduction zones, but this trend is not universal. We do note that the fault valve instability remains unexplored in 3D, where its dynamics are likely more complex, and thus we have no predictions about observed slow slip properties like along-strike migration rate.

6.2 Constraints on hydrological parameters

The fault valve instability is sensitive to several hydrologic parameters, such as flow rate, permeability, specific storage, healing time, and permeability evolution distance. We discuss here how these can be constrained from geological and geophysical observations. The amount of fluid moving up-dip along the megathrust can be estimated. Ther-

modynamic modeling provides estimates of the volume of water released by metamorphic reactions as a function of depth (Peacock, 1990; C. B. Condit et al., 2020; McLellan et al., 2022). The hydration state of the subducting plate can be estimated seismologically (Canales et al., 2017). However, it is more difficult to estimate how much fluid is being diverted into the overriding plate rather than moving along the plate boundary. The flow paths are likely controlled by lithology and the presence or absence of splay faults in the overriding plates (Lauer & Saffer, 2015; Arai et al., 2023). As direct observations are difficult, geodynamic models for geological time-scale subduction are potentially useful to constrain the hydrological structure in the subduction zone (Menant et al., 2019; Wilson et al., 2014; Angiboust et al., 2012; Morishige & van Keken, 2017).

Hyndman et al. (2015) proposed that fluids flow primarily along the plate interface and, after passing the mantle wedge corner, ascend into the overriding plate. Therefore, we compared the simulation results with and without fluid loss at the mantle wedge corner. With fluid loss at the mantle wedge corner, we did not obtain slow slip events and small earthquakes up-dip of the mantle wedge corner, whereas there were active slow slip events and small earthquakes for the case without fluid loss at the mantle wedge corner. The observation in Cascadia is consistent with the fluid sink at the mantle wedge corner, since there is a gap between the locked zone and the region of episodic tremor and slip (Nuyen & Schmidt, 2021).

The flow rate (or Darcy velocity) q depends on the thickness of the fluid transport zone, even if the total volume of fluid moving along the plate boundary is the same. For the same volume rate (per unit distance along-strike) of fluid flow, Q_v, the flow rate $q = Q_v/w$ is inversely proportional to the width of the fluid transport zone. It is important to estimate the extent to which fluid flow is localized using rock records. For example, Ujiie et al. (2018) reports tens of meters thick zones of vein concentration in exhumed subduction zones.

In most slow slip models based on fluids (Perez-Silva et al., 2023; Cruz-Atienza et al., 2018; Skarbek & Rempel, 2016), very high permeability ($k \sim 10^{-12} m^2$) compared to typical values for intact rock ($k \sim 10^{-18} m^2$ (Katayama et al., 2012)) is required to match the migration speed of tremor. Much higher permeabilities than those of intact rock are possible when fractures subparallel to the plate boundary are well connected, as suggested from analysis of mineral veins in the rock record (Hosono et al., 2022; Muñoz-

Montecinos & Behr, 2023). However, field-based approaches could overestimate permeability if the different veins were open at different times. Migration of seismicity also suggests a relatively high permeability (Talwani et al., 2007). However, estimates of permeability from seismic migration might be biased if stress transfer from earthquakes or aseismic slip is neglected, which has been shown to allow slip propagation at a much faster rate than pressure diffusion (Bhattacharya & Viesca, 2019). Thus, in-situ permeability in the slow slip source region is not well understood.

In subduction zones, it is likely that permeability is not a material property, but rather a quantity that dynamically adjusts with variations in the spatial density and connectivity of fractures. An important constraint follows from the fact that the fluid pressure gradient is limited by the lithostatic gradient. Quantitatively,

$$\frac{\partial p}{\partial x} < \rho_r g \sin\theta. \tag{34}$$

Using $q = \frac{k}{\eta}(\frac{\partial p}{\partial x} - \rho_f g \sin\theta)$ and $q = Q_v/w$, we obtain

$$kw > \frac{Q_v \eta}{(\rho_r - \rho_f) g \sin\theta}. \tag{35}$$

Equation (35) illustrates that the product kw (also called hydraulic transmissivity) must be sufficiently large to accommodate the total volume of fluid flowing along the plate boundary that was created by metamorphic dehydration. The channel width may also be a dynamic quantity like permeability that adjusts in order to accommodate the volume rate of fluid flow (that is independently set by the fluid production rate). Specifically, the high fluid pressures in a very narrow channel would create fault-normal pressure gradients that drive fluids outward from the channel. The fluids might then increase the porosity and permeability of the rocks bounding the original channel, thereby expanding the channel. This would reduce the pressure in the channel while maintaining the same volume rate of flow. Ultimately the channel width will adjust to maintain pressures at level below that required for channel expansion by microfracturing and similar processes.

We note that the effect of permeability on the propagation speed of fluid pressure in our model is very different from linear pressure diffusion. As seen from equation (27), the propagation speed scales with the relative permeability enhancement $\Delta k/k_0$. However, as discussed in the previous paragraph, flow rate q_0 and permeability k_0 are not independent. From equations (27) and (35), we have a rough estimate (for $\kappa L_v \ll 1$)

$$V_{phase} \sim \frac{f_0 \Delta k (\rho_r - \rho_f) g \sin\theta}{k_0 \eta \beta \phi a \sigma_0}. \tag{36}$$

Therefore, the phase speed actually scales with Δk and appears to be independent of k_0. However, we note that k_0 affects the background effective normal stress σ_0, with low k_0 generally being associated with low σ_0.

In Model A, the phase speed of fault valve instability for $\lambda = 50$ km is 3×10^{-4} m/s at 30 km depth. On the other hand, the phase speed for linear pressure diffusion is given by $V_{phase(lin)} = c_0\kappa$. Substituting $\lambda = 50$ km and the diffusion coefficient at 30 km depth, $V_{phase(lin)} = 1.2 \times 10^{-5}$ m/s, which is much slower than the phase velocity of fault-valve instability. Thus, fault-valve instability is a much faster mechanism for fluid pressure transport than linear pressure diffusion.

The growth rate and phase velocity of fault valve instability also depend on porosity. The porosity relevant to our model is that of the fluid flow channel rather than the bulk rock. Seismic and electromagnetic imaging are often used to infer the spatial distribution of porosity (Naif et al., 2016; Peacock et al., 2011), but may not be able to resolve meter-scale vein concentration zones. In contrast, exhumed rocks could be used to investigate the permeability and porosity structure of the shear zone. For example, porosities of 1 to 10 % are estimated from rock records in the shear zone at the condition of deep slow earthquakes(Muñoz-Montecinos & Behr, 2023).

6.3 Limitations and future work

Our subduction zone simulations, shown in Figures 11 and 12, have some unrealistic features compared to the Cascadia observations. The duration of each slow slip event is longer than the slow slip recurrence interval. Consequently, part of the fault is always slipping. In contrast, slow slip events at Cascadia have durations of a few weeks and recurrence intervals of about a year (Rogers & Dragert, 2003). It is not currently clear whether this issue can be resolved by changing parameters or whether the model needs to be modified. Future work should test if the model can be tuned to reproduce the various observations of slow slip events and megathrust earthquakes.

We have focused on the slow slip events in the deeper extension of the seismogenic zone. Due to the recent development of seafloor geophysical observations, slow slip events are also detected in the shallow megathrust near the trench (Nakano et al., 2018; Nishikawa et al., 2019). In our megathrust simulations, we did not discuss shallow slow slip events because the fault valve instability in our models due to the choice of the long healing time

in that region. If there are additional healing processes that can operate at these colder temperatures and shallower depth, then shallow slow slip events might also be explained by the fault valve instability.

An important requirement for the fault valve instability is that the pore pressure must be related to the shear strength, and hence slip rate, via the effective stress law. If shear deformation is accommodated by viscous creep with weak pore pressure dependence of viscosity, then a change in pore pressure does not result in a change in slip rate. Models also explain slow slip events based on viscous rheology (Ando et al., 2012), sometimes with thermal coupling (Goswami & Barbot, 2018). However, the existence of seismic signals of slow slip events (i.e., tremor and low frequency earthquakes) suggests that at least part of the deformation in slow slip events is frictional. Field observations of rocks recording deformation at the pressure and temperature conditions of slow earthquakes show heterogeneous structures exhibiting both frictional and viscous deformation (Behr & Bürgmann, 2021). Models simulating both frictional and viscous deformation in the finite thickness shear zone are emerging (Behr et al., 2021), but thus far these neglect fault valving and fluid pressure effects.

Our 2D along-dip simulations do not address the observed along-strike migration of slow slip events. This raises two questions. First, is there background flow in the along-strike direction? Along-strike heterogeneity in dehydration sources related to thermal structure is a possible explanation for its existence (McLellan et al., 2022). Recently, Farge et al. (2023) explained the along-strike migration of tremor by a fault valve type model with along-strike variation of permeability. In contrast, our model focuses on how heterogeneity in permeability and pore pressure arises from internal dynamics starting from a uniform initial state. The two models might be complementary.

Second, even without background flow in the along-strike direction, can 3D dynamics generate along-strike migration of slow slip events? Elastic stress transfer could explain the along-strike migration of slow slip, as discussed by Heimisson et al. (2019). Seismological observations of tremor as diagnostic of slow slip events show that relatively slow along-strike migration of slow slip events is often accompanied by much faster along-dip migration (Ghosh et al., 2010; Obara et al., 2012; Ide, 2012). Several models have attempted to explain this observation. For example, Rubin (2011) proposed a friction law capable of producing a bimodal propagation velocity using two state variables. Ando

et al. (2010) reproduced the difference in migration speed along-strike and along-dip by assuming anisotropic heterogeneity in brittle patches.

The permeability evolution law needs to be elaborated by comparison with experimental observations as well as microphysical modeling. Our model predicts that the steady state permeability is proportional to the slip velocity (6), even away from the steady state, which may overestimate the effect of permeability enhancement. For example, experiments in a granite fracture show much smaller permeability enhancement after velocity jumps than our model (Ishibashi et al., 2018). The permeability evolution law away from the steady state will influence the nonlinear dynamics of the slip pulse, including the peak slip rate.

7 Conclusions

In this work, we studied the dynamics of fault slip with coupling between slip, permeability, fluid flow, and fluid pressure. Using linear stability analysis, we showed that steady slip and fluid flow is unstable to perturbations for sufficiently high background flow rate and degree of permeability enhancement. We identified six dimensionless parameters that control the stability of the system. The fault-valve instability occurs even with pure velocity-strengthening friction, but it is eliminated when the direct effect is removed (i.e., sliding occurs at constant friction coefficient) or the permeability responds instantaneously to the slip velocity. The growth rate and phase speed scale with the permeability enhancement.

Numerical simulations show that the fault valve instability takes the form of unidirectional propagation of an aseismic slip pulse and fluid pressure pulse. The recurrence interval scales with the time scale of permeability evolution, and the propagation velocity and recurrence interval are consistent with the prediction from the linear stability analysis. When the system size is much larger than the preferred wavelength, multiple aseismic slip pulses merge during propagation and the dynamics become more complex.

We have also performed earthquake sequence simulations for subduction megathrusts with depth-dependent parameters. Using the healing time T empirically derived from laboratory experiments and assuming a representative geotherm for subduction zones with deep slow slip events, the simulations spontaneously generated slow slip events (via the fault valve instability) from the lower portion of the seismogenic zone to the down-

dip extension. The slow slip events occur in both velocity-weakening and velocity-strengthening regions. The distributions of effective normal stress and permeability are determined in a self-consistent manner, so we do not have to impose some ad hoc distribution of effective normal stress like in almost all other models for slow slip. Lower permeability near the trench results in lower effective normal stress at the source depth of slow slip. Under this condition, slow slip events have shorter recurrence intervals. The introduction of a fluid sink at the corner of the mantle wedge confines slow slip events to down-dip of the corner and explains the separation between the extent of megathrust rupture and the region of slow slip. This highlights the importance of the determining the amount of fluid discharge into the upper plate.

Some characteristics of slow slip, such as the absence of quiescent periods due to the slow migration rate relative to the recurrence interval and the absence of down-dip migration, are inconsistent with observations in Cascadia. In the future, we plan to study how this instability is manifested in 3D to address both along-dip and along-strike migration of slow slip events. We also plan to relax the certain assumptions made in this study, such as constant porosity and the neglect of fault-normal flow.

Finally, the potential relevance of the fault-valve instability is not limited to subduction zone slow slip events. Aseismic slip is also important for injection-induced seismicity (Bhattacharya & Viesca, 2019). Injection-induced aseismic slip is well studied for constant permeability (Dublanchet, 2019; Sáez et al., 2022), but the fault-valve instability might lead to more complex dynamics.

8 Open Research

The code HBI used in the numerical simulations is found at S. Ozawa (2024b). Other files are found at (S. Ozawa, 2024a).

Appendix A Linear stability analysis

A1 Fluid pressure diffusion equation

The fluid pressure diffusion equation is

$$\beta\phi\frac{\partial p}{\partial t} - \frac{\partial}{\partial x}\left(\frac{k}{\eta}\frac{\partial p}{\partial x}\right) = 0. \tag{A1}$$

We decompose p and k into the superposition of a steady state value and perturbation, denoted with subscript 0 and prime, respectively:

$$\beta\phi\frac{\partial(p_0+p')}{\partial t}-\frac{\partial}{\partial x}\left(\frac{k_0+k'}{\eta}\frac{\partial(p_0+p')}{\partial x}\right)=0. \tag{A2}$$

We assume that k_0 is uniform. Opening brackets and neglecting second-order terms, we obtain

$$\beta\phi\frac{\partial p'}{\partial t}-\frac{k_0}{\eta}\frac{\partial^2 p'}{\partial x^2}+\frac{q_0}{k_0}\frac{\partial k'}{\partial x}=0, \tag{A3}$$

where we made use of the definition of steady flow rate

$$q_0=-\frac{k_0}{\eta}\frac{\partial p_0}{\partial x}. \tag{A4}$$

We Laplace transform time ($\frac{\partial p'}{\partial t}\rightarrow s\hat{p}'$) and Fourier transform in space ($\frac{\partial p'}{\partial x}\rightarrow i\kappa\hat{p}'$). This means we assume $\exp(st+i\kappa x)$ dependence in x and t. Then, we get

$$\beta\phi s\hat{p}'+\frac{k_0}{\eta}\kappa^2\hat{p}'+\frac{q_0}{k_0}i\kappa\hat{k}'=0, \tag{A5}$$

and we denote the hydraulic diffusivity at steady state as c_0:

$$c_0=\frac{k_0}{\beta\phi\eta}. \tag{A6}$$

A2 Permeability evolution equation

We assume that permeability depends on the instantaneous effective normal stress,

$$k=k^* f(\sigma_e) \tag{A7}$$

and the evolution law depends on permeability and slip rate.

$$\frac{dk^*}{dt}=g(k^*,V). \tag{A8}$$

Equations (A7) and (A8) are combined to eliminate k^*, yielding

$$\frac{dk}{dt}=A(k,\sigma_e)\frac{d\sigma_e}{dt}+B(k,\sigma_e,V), \tag{A9}$$

where

$$A(k,\sigma_e)=k\frac{df(\sigma_e)/d\sigma_e}{f(\sigma_e)} \tag{A10}$$

and

$$B(k,\sigma_e,V)=f(\sigma_e)g\left(\frac{k}{f(\sigma_e)},V\right). \tag{A11}$$

Steady state requires $B(k, \sigma_e, V) = 0$, which implicitly defines the steady state permeability function $k = k_{ss}(V, \sigma_e)$.

We denote $k_0 = k_{ss}(V_0, \sigma_0)$ and then linearize equation (A9) and the steady state permeability function $k_{ss}(V, \sigma_e)$ to obtain

$$\frac{dk}{dt} = -\frac{k_0}{\sigma^*}\frac{d\sigma_e}{dt} - \frac{1}{T_k}[k - k_{ss}^{lin}(V, \sigma_e)], \tag{A12}$$

$$k_{ss}(V, \sigma_e) = k_0 - k_0\frac{\sigma_e - \sigma_0}{\sigma^*} + \Delta k\frac{V - V_0}{V_0}, \tag{A13}$$

where we have defined several parameters as follows. The timescale for permeability evolution, T_k, is defined via

$$T_k^{-1} = -\left.\frac{\partial B(k, \sigma_e, V)}{\partial k}\right|_{(k_0, \sigma_0, V_0)}, \tag{A14}$$

the permeability enhancement is

$$\Delta k = V_0\left.\frac{\partial k_{ss}(V, \sigma_e)}{\partial V}\right|_{(V_0, \sigma_0)}, \tag{A15}$$

and the stress sensitivity parameter is

$$\sigma^* = -\frac{k_0}{A(k_0, \sigma_0)} = -\left.\frac{f(\sigma_e)}{df(\sigma_e)/d\sigma_e}\right|_{\sigma_0}. \tag{A16}$$

In the Fourier-Laplace domain, the perturbed variables follow

$$\left(s + \frac{1}{T_k}\right)\hat{k}' = \frac{k_0}{\sigma^*}\left(s + \frac{1}{T_k}\right)\hat{p}' + \frac{\Delta k s\hat{\delta}'}{V_0 T_k}, \tag{A17}$$

where we used $\hat{\delta}' = \hat{V}'/s$ to denote the transform of slip δ.

A3 Rate and state friction and static elasticity

The linearized rate and state friction law is (Rice et al., 2001)

$$\frac{\mathrm{d}\tau}{\mathrm{d}t} = \frac{a\sigma_0}{V_0}\frac{\mathrm{d}V}{\mathrm{d}t} + f_0\frac{\mathrm{d}\sigma_e}{\mathrm{d}t} - \frac{V_0}{d_c}\left[\tau - \tau_{ss}(\sigma_e, V)\right], \tag{A18}$$

where the steady-state shear strength is given by

$$\tau_{ss}(\sigma_e, V) = \tau_0 + f_0(\sigma_e - \sigma_0) + \frac{(a-b)\sigma_0}{V_0}(V - V_0). \tag{A19}$$

In the perturbed state, equations (A18) and (A19) are combined as

$$\frac{\mathrm{d}\tau'}{\mathrm{d}t} = \frac{a\sigma_0}{V_0}\frac{\mathrm{d}V'}{\mathrm{d}t} - f_0\frac{\mathrm{d}p'}{\mathrm{d}t} - \frac{V_0}{d_c}\left[\tau' + f_0 p' - \frac{(a-b)\sigma_0}{V_0}V'\right]. \tag{A20}$$

Performing the Fourier-Laplace transforms and rearranging, we obtain

$$\left(s + \frac{V_0}{d_c}\right)\hat{\tau}' = -f_0\left(s + \frac{V_0}{d_c}\right)\hat{p}' + \sigma_0\left(\frac{a}{V_0}s^2 + \frac{a-b}{d_c}s\right)\hat{\delta}'. \tag{A21}$$

Slip and shear stress are also related by static elasticity (e.g., Rice et al. (2001))

$$\hat{\tau}' = -\frac{\mu^*|\kappa|}{2}\hat{\delta}'. \tag{A22}$$

where $\mu^* = \mu$ for antiplane shear and $\mu^* = \mu/(1-\nu)$ for plane strain.

A4 Characteristic equation

Now we combine equations (A5), (A17), (A21), and (A22) to get

$$\left(s + \frac{V_0}{d_c}\right)\frac{\mu^*}{2}|\kappa| + \sigma_0\left(\frac{a}{V_0}s^2 + \frac{a-b}{d_c}s\right) + \frac{i\kappa f_0 q_0 \Delta k s(s + V_0/d_c)}{k_0\beta\phi V_0 T_k(s + 1/T_k)(s + c_0\kappa^2 + i\kappa q_0/\sigma_0^*\beta\phi)} = 0. \tag{A23}$$

This is an equation that relates the growth rate s and wavenumber κ.

We nondimensionalize the characteristic equation (A23). We take $s = S/T_k$ and rewrite (A23) as

$$PS^2 + \left(\frac{a-b}{a}PJ + 1\right)S + J + iPQ\frac{S(S+J)}{(S+1)(S+R+iM)} = 0. \tag{A24}$$

with five dimensionless parameters defined as follows:

$$P = \frac{2a\sigma_0}{\mu^*|\kappa|V_0 T_k}, \tag{A25}$$

$$Q = \frac{\kappa f_0 q_0 \Delta k T_k}{k_0\beta\phi a\sigma_0}, \tag{A26}$$

$$R = c_0\kappa^2 T_k, \tag{A27}$$

$$M = \frac{\kappa q_0 T_k}{\sigma^*\beta\phi}, \tag{A28}$$

$$J = \frac{V_0 T_k}{d_c}. \tag{A29}$$

See the main text for the physical meaning of these parameters. Note that a/b is the sixth dimensionless parameter of the problem.

If we use a specific permeability evolution law of Zhu et al. (2020),

$$g(k^*, V) = \frac{V}{L}(k_{\max} - k^*) - \frac{1}{T}(k^* - k_{\min}), \tag{A30}$$

and effective stress dependence function

$$f(\sigma_e) = e^{-\sigma_e/\sigma^*}, \tag{A31}$$

then we obtain from (A14) and (A15)

$$T_k^{-1} = 1/T + V_0/L, \tag{A32}$$

$$\Delta k = \frac{V_0 T_k^2 k_{max} e^{-\sigma_0/\sigma^*}}{TL} = \frac{V_0 T_k}{L}\left(k_{max}e^{-\sigma_0/\sigma^*} - k_0\right). \tag{A33}$$

We also note that σ^* coincides with the definition given in (A16).

A5 Limits of negligible state evolution

State evolution is negligible when J is either very large or small. For $J \ll 1$, equation (A24) yields

$$PS + 1 + \frac{iPQS}{(S+1)(S+R+iM)} = 0. \tag{A34}$$

For $J \gg 1$, we divide equation (A24) by J:

$$J^{-1}PS^2 + \left(\frac{a-b}{a}P + J^{-1}\right)S + J + iPQ\frac{S(J^{-1}S+1)}{(S+1)(S+R+iM)} = 0, \tag{A35}$$

and then we assume $J^{-1} \to 0$ to obtain

$$\frac{a-b}{a}PS + 1 + \frac{iPQS}{(S+1)(S+R+iM)} = 0. \tag{A36}$$

In this case, by replacing a with $a - b$ in the definition of P and Q, we recover equation (A34).

Acknowledgments

So Ozawa was partially funded by a Japan Society for the Promotion of Science (JSPS) Overseas Fellowship and Oversea Research Supports from the Yamada Science Foundation. This work was also supported by the National Science Foundation (EAR-1947448 to E.M.D.).

References

Aldam, M., Bar-Sinai, Y., Svetlizky, I., Brener, E. A., Fineberg, J., & Bouchbinder, E. (2016). Frictional sliding without geometrical reflection symmetry. *Physical Review X*, *6*(4), 041023.

Ando, R., Nakata, R., & Hori, T. (2010). A slip pulse model with fault heterogeneity for low-frequency earthquakes and tremor along plate interfaces. *Geophysical Research Letters*, *37*(10).

Ando, R., Takeda, N., & Yamashita, T. (2012). Propagation dynamics of seismic and aseismic slip governed by fault heterogeneity and newtonian rheology. *Journal of Geophysical Research: Solid Earth*, *117*(B11).

Angiboust, S., Wolf, S., Burov, E., Agard, P., & Yamato, P. (2012). Effect of fluid circulation on subduction interface tectonic processes: Insights from thermo-

mechanical numerical modelling. *Earth and Planetary Science Letters*, *357*, 238–248.

Aochi, H., Poisson, B., Toussaint, R., Rachez, X., & Schmittbuhl, J. (2014). Self-induced seismicity due to fluid circulation along faults. *Geophysical Journal International*, *196*(3), 1544–1563.

Arai, R., Miura, S., Nakamura, Y., Fujie, G., Kodaira, S., Kaiho, Y., ... others (2023). Upper-plate conduits linked to plate boundary that hosts slow earthquakes. *Nature Communications*, *14*(1), 5101.

Barbot, S. (2019). Slow-slip, slow earthquakes, period-two cycles, full and partial ruptures, and deterministic chaos in a single asperity fault. *Tectonophysics*, *768*, 228171.

Bar-Sinai, Y., Spatschek, R., Brener, E. A., & Bouchbinder, E. (2014). On the velocity-strengthening behavior of dry friction. *Journal of Geophysical Research: Solid Earth*, *119*(3), 1738–1748.

Bebout, G. E., & Penniston-Dorland, S. C. (2016). Fluid and mass transfer at subduction interfaces—the field metamorphic record. *Lithos*, *240*, 228–258.

Behr, W. M., & Bürgmann, R. (2021). What's down there? the structures, materials and environment of deep-seated slow slip and tremor. *Philosophical Transactions of the Royal Society A*, *379*(2193), 20200218.

Behr, W. M., Gerya, T. V., Cannizzaro, C., & Blass, R. (2021). Transient slow slip characteristics of frictional-viscous subduction megathrust shear zones. *AGU Advances*, *2*(3), e2021AV000416.

Bhattacharya, P., & Viesca, R. C. (2019). Fluid-induced aseismic fault slip outpaces pore-fluid migration. *Science*, *364*(6439), 464–468.

Brantut, N. (2020). Dilatancy-induced fluid pressure drop during dynamic rupture: Direct experimental evidence and consequences for earthquake dynamics. *Earth and Planetary Science Letters*, *538*, 116179.

Brantut, N., & David, E. C. (2019). Influence of fluids on vp/vs ratio: increase or decrease? *Geophysical Journal International*, *216*(3), 2037–2043.

Bürgmann, R. (2018). The geophysics, geology and mechanics of slow fault slip. *Earth and Planetary Science Letters*, *495*, 112–134.

Canales, J. P., Carbotte, S. M., Nedimović, M., & Carton, H. (2017). Dry juan de fuca slab revealed by quantification of water entering cascadia subduction

zone. *Nature Geoscience*, *10*(11), 864–870.

Cappa, F., Guglielmi, Y., & De Barros, L. (2022). Transient evolution of permeability and friction in a slowly slipping fault activated by fluid pressurization. *Nature communications*, *13*(1), 3039.

Chen, J. (2023). The emergence of four types of slow slip cycles on dilatant, fluid saturated faults. *Journal of Geophysical Research: Solid Earth*, *128*(2), e2022JB024382.

Condit, C., & French, M. (2022). Geologic evidence of lithostatic pore fluid pressures at the base of the subduction seismogenic zone. *Geophysical Research Letters*, *49*(12), e2022GL098862.

Condit, C. B., Guevara, V. E., Delph, J. R., & French, M. E. (2020). Slab dehydration in warm subduction zones at depths of episodic slip and tremor. *Earth and Planetary Science Letters*, *552*, 116601.

Cruz-Atienza, V. M., Villafuerte, C., & Bhat, H. S. (2018). Rapid tremor migration and pore-pressure waves in subduction zones. *Nature communications*, *9*(1), 2900.

Dal Zilio, L., & Gerya, T. (2022). Subduction earthquake cycles controlled by episodic fluid pressure cycling. *Lithos*, *426*, 106800.

David, C., Wong, T.-f., Zhu, W., & Zhang, J. (1994). Laboratory measurement of compaction-induced permeability change in porous rocks: Implications for the generation and maintenance of pore pressure excess in the crust. *Pure and applied geophysics*, *143*, 425–456.

Dieterich, J. H. (1979). Modeling of rock friction: 1. experimental results and constitutive equations. *Journal of Geophysical Research: Solid Earth*, *84*(B5), 2161–2168.

Dublanchet, P. (2019). Fluid driven shear cracks on a strengthening rate-and-state frictional fault. *Journal of the Mechanics and Physics of Solids*, *132*, 103672.

Dublanchet, P., & De Barros, L. (2021). Dual seismic migration velocities in seismic swarms. *Geophysical Research Letters*, *48*(1), e2020GL090025.

Dunham, E. M., & Rice, J. R. (2008). Earthquake slip between dissimilar poroelastic materials. *Journal of Geophysical Research: Solid Earth*, *113*(B9).

Farge, G., Jaupart, C., Frank, W. B., & Shapiro, N. M. (2023). Along-strike segmentation of seismic tremor and its relationship with the hydraulic structure of the

subduction fault zone. *Journal of Geophysical Research: Solid Earth*, *128*(12), e2023JB027584.

Farge, G., Jaupart, C., & Shapiro, N. M. (2021). Episodicity and migration of low frequency earthquakes modeled with fast fluid pressure transients in the permeable subduction interface. *Journal of Geophysical Research: Solid Earth*, *126*(9), e2021JB021894.

Faulkner, D., Jackson, C., Lunn, R., Schlische, R., Shipton, Z., Wibberley, C., & Withjack, M. (2010). A review of recent developments concerning the structure, mechanics and fluid flow properties of fault zones. *Journal of Structural Geology*, *32*(11), 1557–1575.

Fisher, D., Smye, A., Marone, C., Van Keken, P., & Yamaguchi, A. (2019). Kinetic models for healing of the subduction interface based on observations of ancient accretionary complexes. *Geochemistry, Geophysics, Geosystems*, *20*(7), 3431–3449.

Gao, H., Schmidt, D. A., & Weldon, R. J. (2012). Scaling relationships of source parameters for slow slip events. *Bulletin of the Seismological Society of America*, *102*(1), 352–360.

Ghosh, A., Vidale, J. E., Sweet, J. R., Creager, K. C., Wech, A. G., Houston, H., & Brodsky, E. E. (2010). Rapid, continuous streaking of tremor in cascadia. *Geochemistry, Geophysics, Geosystems*, *11*(12).

Giger, S. B., Tenthorey, E., Cox, S. F., & Fitz Gerald, J. D. (2007). Permeability evolution in quartz fault gouges under hydrothermal conditions. *Journal of Geophysical Research: Solid Earth*, *112*(B7).

Gosselin, J. M., Audet, P., Estève, C., McLellan, M., Mosher, S. G., & Schaeffer, A. J. (2020). Seismic evidence for megathrust fault-valve behavior during episodic tremor and slip. *Science Advances*, *6*(4), eaay5174.

Goswami, A., & Barbot, S. (2018). Slow-slip events in semi-brittle serpentinite fault zones. *Scientific reports*, *8*(1), 6181.

Hacker, B. R., Peacock, S. M., Abers, G. A., & Holloway, S. D. (2003). Subduction factory 2. are intermediate-depth earthquakes in subducting slabs linked to metamorphic dehydration reactions? *Journal of Geophysical Research: Solid Earth*, *108*(B1).

Hawthorne, J. C., & Rubin, A. M. (2013). Laterally propagating slow slip events

in a rate and state friction model with a velocity-weakening to velocity-strengthening transition. *Journal of Geophysical Research: Solid Earth*, *118*(7), 3785–3808.

Heimisson, E. R., Dunham, E. M., & Almquist, M. (2019). Poroelastic effects destabilize mildly rate-strengthening friction to generate stable slow slip pulses. *Journal of the Mechanics and Physics of Solids*, *130*, 262–279.

Heimisson, E. R., Liu, S., Lapusta, N., & Rudnicki, J. (2022). A spectral boundary-integral method for faults and fractures in a poroelastic solid: Simulations of a rate-and-state fault with dilatancy, compaction, and fluid injection. *Journal of Geophysical Research: Solid Earth*, *127*(9), e2022JB024185.

Heimisson, E. R., Rudnicki, J., & Lapusta, N. (2021). Dilatancy and compaction of a rate-and-state fault in a poroelastic medium: Linearized stability analysis. *Journal of Geophysical Research: Solid Earth*, *126*(8), e2021JB022071.

Hooker, J., & Fisher, D. (2021). How cementation and fluid flow influence slip behavior at the subduction interface. *Geology*, *49*(9), 1074–1078.

Hosono, H., Takemura, T., Asahina, D., & Otsubo, M. (2022). Estimation of paleo-permeability around a seismogenic fault based on permeability tensor from observable geometric information of quartz veins. *Earth, Planets and Space*, *74*(1), 141.

Hyndman, R. D., McCrory, P. A., Wech, A., Kao, H., & Ague, J. (2015). Cascadia subducting plate fluids channelled to fore-arc mantle corner: Ets and silica deposition. *Journal of Geophysical Research: Solid Earth*, *120*(6), 4344–4358.

Ide, S. (2012). Variety and spatial heterogeneity of tectonic tremor worldwide. *Journal of Geophysical Research: Solid Earth*, *117*(B3).

Im, K., Elsworth, D., & Wang, C. (2019). Cyclic permeability evolution during repose then reactivation of fractures and faults. *Journal of Geophysical Research: Solid Earth*, *124*(5), 4492–4506.

Im, K., Saffer, D., Marone, C., & Avouac, J.-P. (2020). Slip-rate-dependent friction as a universal mechanism for slow slip events. *Nature Geoscience*, *13*(10), 705–710.

Ingebritsen, S. E., & Manning, C. (2010). Permeability of the continental crust: dynamic variations inferred from seismicity and metamorphism. *Geofluids*, *10*(1-2), 193–205.

Ishibashi, T., Elsworth, D., Fang, Y., Riviere, J., Madara, B., Asanuma, H., ... Marone, C. (2018). Friction-stability-permeability evolution of a fracture in granite. *Water Resources Research*, *54*(12), 9901–9918.

Kaneki, S., & Noda, H. (2023). Steady-state effective normal stress in subduction zones based on hydraulic models and implications for shallow slow earthquakes. *Journal of Geophysical Research: Solid Earth*, *128*(2), e2022JB025995.

Katayama, I., Terada, T., Okazaki, K., & Tanikawa, W. (2012). Episodic tremor and slow slip potentially linked to permeability contrasts at the moho. *Nature Geoscience*, *5*(10), 731–734.

Kato, N. (2003). A possible model for large preseismic slip on a deeper extension of a seismic rupture plane. *Earth and Planetary Science Letters*, *216*(1-2), 17–25.

Kawano, S., Katayama, I., & Okazaki, K. (2011). Permeability anisotropy of serpentinite and fluid pathways in a subduction zone. *Geology*, *39*(10), 939–942.

Kennedy, B., Kharaka, Y., Evans, W. C., Ellwood, A., DePaolo, D., Thordsen, J., ... Mariner, R. (1997). Mantle fluids in the san andreas fault system, california. *Science*, *278*(5341), 1278–1281.

Kodaira, S., Iidaka, T., Kato, A., Park, J.-O., Iwasaki, T., & Kaneda, Y. (2004). High pore fluid pressure may cause silent slip in the nankai trough. *Science*, *304*(5675), 1295–1298.

Lauer, R. M., & Saffer, D. M. (2015). The impact of splay faults on fluid flow, solute transport, and pore pressure distribution in subduction zones: A case study offshore the n icoya p eninsula, c osta r ica. *Geochemistry, Geophysics, Geosystems*, *16*(4), 1089–1104.

Li, D., & Liu, Y. (2016). Spatiotemporal evolution of slow slip events in a nonplanar fault model for northern cascadia subduction zone. *Journal of Geophysical Research: Solid Earth*, *121*(9), 6828–6845.

Linker, M., & Dieterich, J. H. (1992). Effects of variable normal stress on rock friction: Observations and constitutive equations. *Journal of Geophysical Research: Solid Earth*, *97*(B4), 4923–4940.

Liu, Y., & Rice, J. R. (2007). Spontaneous and triggered aseismic deformation transients in a subduction fault model. *Journal of Geophysical Research: Solid*

Earth, *112*(B9).

Liu, Y., & Rubin, A. M. (2010). Role of fault gouge dilatancy on aseismic deformation transients. *Journal of Geophysical Research: Solid Earth*, *115*(B10).

Lockner, D. A., Tanaka, H., Ito, H., Ikeda, R., Omura, K., & Naka, H. (2009). Geometry of the nojima fault at nojima-hirabayashi, japan–i. a simple damage structure inferred from borehole core permeability. *Pure and Applied Geophysics*, *166*, 1649–1667.

Luo, Y., & Liu, Z. (2021). Fault zone heterogeneities explain depth-dependent pattern and evolution of slow earthquakes in cascadia. *Nature Communications*, *12*(1), 1959.

Marguin, V., & Simpson, G. (2023). Influence of fluids on earthquakes based on numerical modeling. *Journal of Geophysical Research: Solid Earth*, *128*(2), e2022JB025132.

Marone, C. (1998). Laboratory-derived friction laws and their application to seismic faulting. *Annual Review of Earth and Planetary Sciences*, *26*(1), 643–696.

Matsumoto, Y., Yoshida, K., Matsuzawa, T., & Hasegawa, A. (2021). Fault-valve behavior estimated from intensive foreshocks and aftershocks of the 2017 m 5.3 kagoshima bay earthquake sequence, kyushu, southern japan. *Journal of Geophysical Research: Solid Earth*, *126*(5), e2020JB020278.

Matsuzawa, T., Shibazaki, B., Obara, K., & Hirose, H. (2013). Comprehensive model of short-and long-term slow slip events in the shikoku region of japan, incorporating a realistic plate configuration. *Geophysical Research Letters*, *40*(19), 5125–5130.

Mattsson, K. (2012). Summation by parts operators for finite difference approximations of second-derivatives with variable coefficients. *Journal of Scientific Computing*, *51*(3), 650–682.

Mavko, G., Mukerji, T., & Dvorkin, J. (2020). *The rock physics handbook*. Cambridge university press.

McLellan, M., Audet, P., Rosas, J. C., & Currie, C. (2022). Margin-wide variations in slab dehydration in cascadia and their relationship to slow slip. *Lithos*, *434*, 106912.

Menant, A., Angiboust, S., & Gerya, T. (2019). Stress-driven fluid flow controls long-term megathrust strength and deep accretionary dynamics. *Scientific re-*

ports, *9*(1), 9714.

Mitchell, T., & Faulkner, D. (2012). Towards quantifying the matrix permeability of fault damage zones in low porosity rocks. *Earth and Planetary Science Letters*, *339*, 24–31.

Morishige, M., & van Keken, P. E. (2017). Along-arc variation in short-term slow slip events caused by 3-d fluid migration in subduction zones. *Journal of Geophysical Research: Solid Earth*, *122*(2), 1434–1448.

Morrow, C. A., Moore, D. E., & Lockner, D. (2001). Permeability reduction in granite under hydrothermal conditions. *Journal of Geophysical Research: Solid Earth*, *106*(B12), 30551–30560.

Muñoz-Montecinos, J., & Behr, W. M. (2023). Transient permeability of a deep-seated subduction interface shear zone. *Geophysical Research Letters*, *50*(20), e2023GL104244.

Naif, S., Key, K., Constable, S., & Evans, R. L. (2016). Porosity and fluid budget of a water-rich megathrust revealed with electromagnetic data at the m iddle a merica t rench. *Geochemistry, Geophysics, Geosystems*, *17*(11), 4495–4516.

Nakano, M., Hori, T., Araki, E., Kodaira, S., & Ide, S. (2018). Shallow very-low-frequency earthquakes accompany slow slip events in the nankai subduction zone. *Nature communications*, *9*(1), 984.

Nie, S., & Barbot, S. (2021). Seismogenic and tremorgenic slow slip near the stability transition of frictional sliding. *Earth and Planetary Science Letters*, *569*, 117037.

Nishikawa, T., Matsuzawa, T., Ohta, K., Uchida, N., Nishimura, T., & Ide, S. (2019). The slow earthquake spectrum in the japan trench illuminated by the s-net seafloor observatories. *Science*, *365*(6455), 808–813.

Nishiyama, N., Sumino, H., & Ujiie, K. (2020). Fluid overpressure in subduction plate boundary caused by mantle-derived fluids. *Earth and Planetary Science Letters*, *538*, 116199.

Noda, H., & Lapusta, N. (2010). Three-dimensional earthquake sequence simulations with evolving temperature and pore pressure due to shear heating: Effect of heterogeneous hydraulic diffusivity. *Journal of Geophysical Research: Solid Earth*, *115*(B12).

Nuyen, C. P., & Schmidt, D. A. (2021). Filling the gap in cascadia: The emergence

of low-amplitude long-term slow slip. *Geochemistry, Geophysics, Geosystems*, *22*(3), e2020GC009477.

Obara, K. (2010). Phenomenology of deep slow earthquake family in southwest japan: Spatiotemporal characteristics and segmentation. *Journal of Geophysical Research: Solid Earth*, *115*(B8).

Obara, K., Matsuzawa, T., Tanaka, S., & Maeda, T. (2012). Depth-dependent mode of tremor migration beneath kii peninsula, nankai subduction zone. *Geophysical Research Letters*, *39*(10).

Okuda, H., Kitamura, M., Takahashi, M., & Yamaguchi, A. (2023). Frictional properties of the décollement in the shallow nankai trough: constraints from friction experiments simulating in-situ conditions and implications for the seismogenic zone. *Earth and Planetary Science Letters*, *621*, 118357.

Otsubo, M., Hardebeck, J. L., Miyakawa, A., Yamaguchi, A., & Kimura, G. (2020). Localized fluid discharge by tensile cracking during the post-seismic period in subduction zones. *Scientific Reports*, *10*(1), 12281.

Ozawa, S. (2024a, March). *Scripts used to produce the results presented in ozawa et al. (2024).* Stanford Digital Repository. Retrieved from `https://doi.org/10.25740/bq498cn4340` doi: doi.org/10.25740/bq498cn4340

Ozawa, S. (2024b, March). *sozawa94/hbi: Faultvalve2d.* Zenodo. Retrieved from `https://doi.org/10.5281/zenodo.10855266` doi: 10.5281/zenodo.10855266

Ozawa, S., Ida, A., Hoshino, T., & Ando, R. (2023). Large-scale earthquake sequence simulations on 3-d non-planar faults using the boundary element method accelerated by lattice h-matrices. *Geophysical Journal International*, *232*(3), 1471–1481.

Ozawa, S. W., Hatano, T., & Kame, N. (2019). Longer migration and spontaneous decay of aseismic slip pulse caused by fault roughness. *Geophysical Research Letters*, *46*(2), 636–643.

Peacock, S. M. (1990). Fluid processes in subduction zones. *Science*, *248*(4953), 329–337.

Peacock, S. M., Christensen, N. I., Bostock, M. G., & Audet, P. (2011). High pore pressures and porosity at 35 km depth in the cascadia subduction zone. *Geology*, *39*(5), 471–474.

Perez-Silva, A., Kaneko, Y., Savage, M., Wallace, L., & Warren-Smith, E. (2023). Characteristics of slow slip events explained by rate-strengthening faults subject to periodic pore fluid pressure changes. *Journal of Geophysical Research: Solid Earth*, *128*(6), e2022JB026332.

Perfettini, H., & Molinari, A. (2023). The interaction between frictional slip and viscous fault root produces slow slip events. *Journal of Geophysical Research: Solid Earth*, *128*(3), e2022JB024645.

Petrini, C., Gerya, T., Yarushina, V., van Dinther, Y., Connolly, J., & Madonna, C. (2020). Seismo-hydro-mechanical modelling of the seismic cycle: Methodology and implications for subduction zone seismicity. *Tectonophysics*, *791*, 228504.

Press, W., Tenkolsky, W., et al. (2002). *Numerical recipes in fortran 90: The art of parralel scientific compputing.* University Press Cambrige.

Proctor, B., Lockner, D. A., Kilgore, B. D., Mitchell, T. M., & Beeler, N. M. (2020). Direct evidence for fluid pressure, dilatancy, and compaction affecting slip in isolated faults. *Geophysical Research Letters*, *47*(16), e2019GL086767.

Ranjith, K. (2014). Instabilities in dynamic anti-plane sliding of an elastic layer on a dissimilar elastic half-space. *Journal of Elasticity*, *115*(1), 47–59.

Rice, J. R. (1992). Fault stress states, pore pressure distributions, and the weakness of the san andreas fault. In *International geophysics* (Vol. 51, pp. 475–503). Elsevier.

Rice, J. R. (1993). Spatio-temporal complexity of slip on a fault. *Journal of Geophysical Research: Solid Earth*, *98*(B6), 9885–9907.

Rice, J. R. (2006). Heating and weakening of faults during earthquake slip. *Journal of Geophysical Research: Solid Earth*, *111*(B5).

Rice, J. R., Lapusta, N., & Ranjith, K. (2001). Rate and state dependent friction and the stability of sliding between elastically deformable solids. *Journal of the Mechanics and Physics of Solids*, *49*(9), 1865–1898.

Rogers, G., & Dragert, H. (2003). Episodic tremor and slip on the cascadia subduction zone: The chatter of silent slip. *Science*, *300*(5627), 1942–1943.

Romanet, P., Bhat, H. S., Jolivet, R., & Madariaga, R. (2018). Fast and slow slip events emerge due to fault geometrical complexity. *Geophysical Research Letters*, *45*(10), 4809–4819.

Ross, Z. E., Cochran, E. S., Trugman, D. T., & Smith, J. D. (2020). 3d fault ar-

chitecture controls the dynamism of earthquake swarms. *Science*, *368*(6497), 1357–1361.

Rubin, A. M. (2008). Episodic slow slip events and rate-and-state friction. *Journal of Geophysical Research: Solid Earth*, *113*(B11).

Rubin, A. M. (2011). Designer friction laws for bimodal slow slip propagation speeds. *Geochemistry, Geophysics, Geosystems*, *12*(4).

Ruina, A. (1983). Slip instability and state variable friction laws. *Journal of Geophysical Research: Solid Earth*, *88*(B12), 10359–10370.

Sáez, A., Lecampion, B., Bhattacharya, P., & Viesca, R. C. (2022). Three-dimensional fluid-driven stable frictional ruptures. *Journal of the Mechanics and Physics of Solids*, *160*, 104754.

Saffer, D. M. (2012). The permeability of active subduction plate boundary faults. *Crustal Permeability*, 207–227.

Saffer, D. M., & Tobin, H. J. (2011). Hydrogeology and mechanics of subduction zone forearcs: Fluid flow and pore pressure. *Annual Review of Earth and Planetary Sciences*, *39*, 157–186.

Saishu, H., Okamoto, A., & Otsubo, M. (2017). Silica precipitation potentially controls earthquake recurrence in seismogenic zones. *Scientific reports*, *7*(1), 13337.

Sakamoto, R., & Tanaka, Y. (2022). Frictional and hydraulic properties of plate interfaces constrained by a tidal response model considering dilatancy/compaction. *Journal of Geophysical Research: Solid Earth*, *127*(8), e2022JB024112.

Scholz, C. H. (1998). Earthquakes and friction laws. *Nature*, *391*(6662), 37–42.

Segall, P. (2010). *Earthquake and volcano deformation*. Princeton University Press.

Segall, P., Rubin, A. M., Bradley, A. M., & Rice, J. R. (2010). Dilatant strengthening as a mechanism for slow slip events. *Journal of Geophysical Research: Solid Earth*, *115*(B12).

Shelly, D. R., Ellsworth, W. L., & Hill, D. P. (2016). Fluid-faulting evolution in high definition: Connecting fault structure and frequency-magnitude variations during the 2014 long valley caldera, california, earthquake swarm. *Journal of Geophysical Research: Solid Earth*, *121*(3), 1776–1795.

Shibazaki, B., & Iio, Y. (2003). On the physical mechanism of silent slip events

along the deeper part of the seismogenic zone. *Geophysical Research Letters*, *30*(9).

Shimamoto, T. (1986). Transition between frictional slip and ductile flow for halite shear zones at room temperature. *Science*, *231*(4739), 711–714.

Shreedharan, S., Ikari, M., Wood, C., Saffer, D., Wallace, L., & Marone, C. (2022). Frictional and lithological controls on shallow slow slip at the northern hikurangi margin. *Geochemistry, Geophysics, Geosystems*, *23*(2), e2021GC010107.

Sibson, R. (1992). Implications of fault-valve behaviour for rupture nucleation and recurrence. *Tectonophysics*, *211*(1-4), 283–293.

Skarbek, R. M., & Rempel, A. W. (2016). Dehydration-induced porosity waves and episodic tremor and slip. *Geochemistry, Geophysics, Geosystems*, *17*(2), 442–469.

Skarbek, R. M., Rempel, A. W., & Schmidt, D. A. (2012). Geologic heterogeneity can produce aseismic slip transients. *Geophysical Research Letters*, *39*(21).

Skarbek, R. M., & Saffer, D. M. (2009). Pore pressure development beneath the décollement at the nankai subduction zone: Implications for plate boundary fault strength and sediment dewatering. *Journal of Geophysical Research: Solid Earth*, *114*(B7).

Talwani, P., Chen, L., & Gahalaut, K. (2007). Seismogenic permeability, ks. *Journal of Geophysical Research: Solid Earth*, *112*(B7).

Tanaka, Y., Suzuki, T., Imanishi, Y., Okubo, S., Zhang, X., Ando, M., ... others (2018). Temporal gravity anomalies observed in the tokai area and a possible relationship with slow slips. *Earth, Planets and Space*, *70*, 1–8.

Tarling, M. S., Smith, S. A., & Scott, J. M. (2019). Fluid overpressure from chemical reactions in serpentinite within the source region of deep episodic tremor. *Nature Geoscience*, *12*(12), 1034–1042.

Thomas, A., Bürgmann, R., Shelly, D. R., Beeler, N. M., & Rudolph, M. (2012). Tidal triggering of low frequency earthquakes near parkfield, california: Implications for fault mechanics within the brittle-ductile transition. *Journal of Geophysical Research: Solid Earth*, *117*(B5).

Tse, S. T., & Rice, J. R. (1986). Crustal earthquake instability in relation to the depth variation of frictional slip properties. *Journal of Geophysical Research: Solid Earth*, *91*(B9), 9452–9472.

Ujiie, K., Saishu, H., Fagereng, Å., Nishiyama, N., Otsubo, M., Masuyama, H., & Kagi, H. (2018). An explanation of episodic tremor and slow slip constrained by crack-seal veins and viscous shear in subduction mélange. *Geophysical Research Letters*, *45*(11), 5371–5379.

Van Keken, P. E., Hacker, B. R., Syracuse, E. M., & Abers, G. A. (2011). Subduction factory: 4. depth-dependent flux of h2o from subducting slabs worldwide. *Journal of Geophysical Research: Solid Earth*, *116*(B1).

Warren-Smith, E., Fry, B., Wallace, L., Chon, E., Henrys, S., Sheehan, A., ... Lebedev, S. (2019). Episodic stress and fluid pressure cycling in subducting oceanic crust during slow slip. *Nature Geoscience*, *12*(6), 475–481.

Wech, A. G., & Creager, K. C. (2011). A continuum of stress, strength and slip in the cascadia subduction zone. *Nature Geoscience*, *4*(9), 624–628.

Wibberley, C. A., & Shimamoto, T. (2003). Internal structure and permeability of major strike-slip fault zones: the median tectonic line in mie prefecture, southwest japan. *Journal of Structural Geology*, *25*(1), 59–78.

Williams, R. T., & Fagereng, Å. (2022). The role of quartz cementation in the seismic cycle: A critical review. *Reviews of Geophysics*, *60*(1), e2021RG000768.

Wilson, C. R., Spiegelman, M., van Keken, P. E., & Hacker, B. R. (2014). Fluid flow in subduction zones: The role of solid rheology and compaction pressure. *Earth and Planetary Science Letters*, *401*, 261–274.

Xue, L., Li, H.-B., Brodsky, E. E., Xu, Z.-Q., Kano, Y., Wang, H., ... others (2013). Continuous permeability measurements record healing inside the wenchuan earthquake fault zone. *Science*, *340*(6140), 1555–1559.

Yamashita, T. (2013). Generation of slow slip coupled with tremor due to fluid flow along a fault. *Geophysical Journal International*, *193*(1), 375–393.

Yang, Y., & Dunham, E. M. (2021). Effect of porosity and permeability evolution on injection-induced aseismic slip. *Journal of Geophysical Research: Solid Earth*, *126*(7), e2020JB021258.

Yang, Y., & Dunham, E. M. (2023). Influence of creep compaction and dilatancy on earthquake sequences and slow slip. *Journal of Geophysical Research: Solid Earth*, *128*(4), e2022JB025969.

Yehya, A., & Rice, J. R. (2020). Influence of fluid-assisted healing on fault permeability structure. *Journal of Geophysical Research: Solid Earth*, *125*(10),

e2020JB020553.

Zhu, W., Allison, K. L., Dunham, E. M., & Yang, Y. (2020). Fault valving and pore pressure evolution in simulations of earthquake sequences and aseismic slip. *Nature communications*, *11*(1), 4833.

Zhu, W., & Wong, T.-f. (1997). The transition from brittle faulting to cataclastic flow: Permeability evolution. *Journal of Geophysical Research: Solid Earth*, *102*(B2), 3027–3041.